THE ASTROPHYSICAL JOURNAL, 472:460–484, 1996 December 1

GALAXY DYNAMICS IN CLUSTERS

CARLOS S. FRENK[1]
Department of Physics, University of Durham, South Road, Durham DH1 3LE England, UK
AUGUST E. EVRARD[1]
Department of Physics, University of Michigan, Ann Arbor, M1 48109-1120
SIMON D. M. WHITE[1]
Max-Planck-Institut für Astrophysik, Karl-Schwarzschild-Strasse 1, D-8046 Garching bei München, Germany
AND
F. J. SUMMERS
Department of Astrophysical Sciences, Princeton University, Princeton, NJ 08544
Received 1995 March 15; accepted 1996 June 14

ABSTRACT

We use high-resolution simulations to study the formation and distribution of galaxies within a cluster that forms hierarchically. We follow both dark matter and a gas component that is subject to thermal pressure, shocks, and radiative cooling. Galaxy formation is identified with the dissipative collapse of the gas into cold, compact knots. We explore two extreme numerical representations of these galaxies during subsequent cluster evolution, one purely gaseous and the other purely stellar, and we find that the results are quite sensitive to this choice. Simulations in which galaxies remain gaseous appear to suffer from an "overmerging" problem, but this problem is much less severe if the gas is allowed to turn into stars. We compare the kinematics of the galaxy population in these two representations to the kinematics of dark halos and of the underlying dark matter distribution. Galaxies in the stellar representation are positively biased (i.e., overrepresented in the cluster) both by number and by mass fraction. Both representations predict the galaxies to be more centrally concentrated than the dark matter, whereas the dark halo population is more extended. A modest velocity bias also exists in both representations, with the largest effect, $\sigma_{\rm gal}/\sigma_{\rm DM} \simeq 0.7$, found for the more massive star galaxies. Phase diagrams show that the galaxy population in the stellar case is roughly in hydrostatic equilibrium. Virial mass estimators can underestimate the true cluster mass by up to a factor of 5 because of these various bias effects. The discrepancy is largest if only the most massive galaxies are used, reflecting significant mass segregation. A binding energy analysis suggests that this segregation is primarily a result of dynamical friction. We discuss briefly the relevance of these results both to real clusters and to the general problem of simulating the formation and clustering of galaxies. The incorporation of a realistic star formation algorithm within future simulations is the key to further progress.

Subject headings: dark matter — galaxies: clusters: general — galaxies: halos — methods: numerical

1. INTRODUCTION

Galaxy clusters play a central role in cosmological studies. As the most massive nonlinear structures in the universe, they have been used to estimate the mean cosmic mass density and to constrain the nature of the dark matter. As young objects whose dynamical timescale is a large fraction of the age of the universe, they have been used to probe the initial conditions for structure formation.

Clusters are multicomponent systems in which dark matter, hot gas, and galaxies evolve in a tightly coupled way. Their study is best approached through direct numerical simulation, but such simulations must include the proper cosmological context for cluster formation, as well as an appropriate representation of the three principal constituents and their interactions. In this paper we use simulations to explore the physical processes that establish the multicomponent nature of clusters, the mechanisms that determine the final distributions of the different components, and the extent to which nonlinear dynamical effects may prejudice the use of clusters as cosmological tools.

Simulations of cluster formation have increased gradually in complexity. Early N-body studies, beginning with Peebles (1970) and White (1976), concentrated on the collapse and relaxation of the dark matter component and on possible segregation effects acting on the most massive galaxies. Later work considered how the structure of clusters is related to the cosmological context in which they form (Quinn, Salmon, & Zurek 1986; West, Dekel & Oemler 1987; Evrard 1987; White et al. 1987b; Efstathiou et al. 1988; Frenk et al. 1990; Crone, Evrard, & Richstone 1994). Overdense regions separate from the general expansion, and the subsequent collapse destroys their clumpy initial structure to produce smooth, centrally concentrated configurations that are close to virial equilibrium. Incomplete relaxation at intermediate times can result in substantial apparent substructure that may be used as an observational estimator of the cosmic density parameter, Ω (Richstone, Loeb, & Turner 1992; Kauffmann & White 1993; Lacey & Cole 1993; Evrard et al. 1993; Wilson, Cole, & Frenk 1996).

[1] Institute for Theoretical Physics, University of California, Santa Barbara, CA 93106-4030.

The next level of complexity in cluster simulations was achieved through the inclusion of a collisional component to represent the intracluster gas. In the first such models, hydrodynamic processes were included rather crudely by allowing inelastic collisions between gas particles (Carlberg 1988; Carlberg & Couchman 1989). Since large spatial and temporal variations in density occur during cluster evolution, the "smooth particle hydrodynamics" (SPH) technique proves well suited to this problem. Simulations by Evrard (1990) and Thomas & Couchman (1992) using P^3M/SPH codes, and simulatons by Tsai, Katz, & Bertschinger (1994) and by Navarro, Frenk, & White (1995) using tree/SPH codes, showed that the collapse and shock heating of a *nonradiative* gas leads to final cluster states whose X-ray emission resembles that seen in real clusters.

Neither N-body nor nonradiative SPH simulations treat processes related to the presence of galaxies in clusters. Although visible stars represent a negligible fraction of the total cluster mass (and only a small fraction of the directly observed mass; e.g., White et al. 1993), it is evident that such processes should be included in any realistic cluster model. Some attempts have been made to study the effects of biased galaxy formation, dynamical friction, galaxy mergers, and metal enrichment, either by inserting heavy "galaxy particles" by hand into the initial conditions (Evrard 1987; West & Richstone 1988) or by identifying their initial locations with high peaks of the linear overdensity field (White et al. 1987b; Metzler & Evrard 1994). These calculations provide useful dynamical insights, but they sidestep many issues concerning how galaxy and cluster formation are coupled. To address these questions, it is necessary to include additional physics, primarily cooling, in an explicit way. This is done most directly by carrying out much larger simulations that have sufficient dynamic range to follow both the dissipative collapse of the galaxies and the subsequent formation of the cluster by hierarchical clustering. Such an investigation is the subject of this paper.

So far only a few cosmological N-body/SPH simulations have been published that include the effects of radiative cooling. The first was used by Carlberg, Couchman, & Thomas (1990) to establish the concept of velocity bias. Katz, Hernquist, & Weinberg (1992) explored galaxy formation in their study of evolution within a relatively small region (22 Mpc^2) of a universe dominated by cold dark matter (CDM). Evrard, Summers, & Davis (1994) carried out a higher resolution simulation and chose their computational box (of side 16 Mpc) to enclose the expected formation site of a poor group in a CDM universe. Together with the simulation of Katz et al. (1992), a lower resolution simulation by Katz & White (1993), and the "sticky particle" simulations of Carlberg & Couchman (1989), this work illustrates how cooling results in the formation of dense gas clumps that can survive the disruption of their halos within clusters. Thus, it supports the original conjecture of White & Rees (1978) that dissipative effects within hierarchical clustering theories can explain the existence of virialized clusters containing many distinct galaxies.

An alternative approach to simulating the dynamics of gas in a cosmological context is being pursued by several groups (e.g., Cen & Ostriker 1992a, 1992b; Roettinger, Burns, & Loken 1993; Kang et al. 1994; Bryan et al. 1994). This work uses finite difference techniques to follow the dynamics of a fluid that can undergo radiative heating and cooling and is allowed to turn into stars. Such grid-based methods are particularly useful for studying the large-scale gas distribution and for following dynamical effects in the neighborhood of shocks. However, the schemes used so far have had insufficient resolution to follow the details of cluster formation in a proper cosmological context or to simulate the formation and clustering of galaxies.

In this paper, we discuss results from new P3MSPH simulations that have a number of features in common with the model of Evrard et al. (1994, hereafter ESD). Like these authors, we follow the evolution of an initially overdense region, but we choose one that forms a rich cluster like Coma rather than a poor group, and we lay down initial conditions in a different way. Our simulation has lower resolution than theirs, but we are able to follow evolution to $z = 0$, rather than to $z = 1$ as they did because of CPU limitations. Furthermore, whereas ESD considered the evolution of gaseous galaxies only, we concentrate on how the dynamics of the galaxy population within the cluster depend on the way in which galaxies are modeled. In particular, we compare results for two extreme cases, one in which no star formation occurs in the cold dense clumps that are taken to represent galaxies, and the other in which these clumps are turned into stars at an epoch well before cluster collapse. The differences between these two treatments turn out to be large. Although extreme, these two possibilities bracket an interesting range of behavior relevant to galaxies in real clusters. Such experimentation is a prerequisite for more complex modeling, including phenomena such as self-consistent star formation and associated feedback processes.

The rest of this paper is organized as follows. In § 2 we describe our simulation techniques and our procedure for generating initial condition. In § 3 we present an overview of the dynamical evolution of the cluster, including images to illustrate its global properties, and we quantify the abundance of galaxies in the simulation. In § 4 we discuss the structure of the cluster, the orbits, and merger rates of the galaxies that form, and we investigate their hydrodynamical equilibrium. We analyze the evolution of the binding energy of galaxies and cluster dark matter and use this as a tool to understand the physical origin of various biases present in the cluster populations. Then we assess the accuracy of virial mass estimates and their implications for estimates of the mean cosmic density. Our paper concludes with a discussion of the main results in § 5.

2. THE SIMULATIONS

We use the P3MSPH code described by Evrard (1988; see also Efstathiou et al. 1985 and Summers 1993) to model the evolution of 524,288 particles. Half of them interact only through gravity and represent the dark matter, and half of them experience both gravity and hydrodynamic forces and represent the gas. The gas is able to undergo adiabatic compression and shocks (as a result of an artificial viscosity term included in the hydrodynamic equations) and can cool radiatively, at a rate that depends on density and temperature according to the cooling function appropriate to an optically thin plasma of primordial composition in collisional ionization equilibrium. (The cooling function includes the effects of thermal bremsstrahlung, radiative

[2] We write Hubble's constant as $H_0 = 100\ h^{-1}$ Mpc and, unless otherwise stated, we take $h = 0.5$.

recombination, dielectronic recombination, and line emission, but not of heating by photoionization. This may be important on scales smaller than those we can resolve in our simulations; Efstathiou 1992, Katz, Hernquist, & Weinberg 1995). The gasdynamic simulations described below were carried out in 1992 using the Cray YMP8 at the San Diego Supercomputer Center and took roughly 150 hours of CPU time each.

2.1. *Initial Conditions and Numerical Parameters*

Our procedure for laying down initial conditions is designed to extend the dynamic range accessible to a single cosmological calculation and imposes a cluster perturbation in two basic steps. First we identify a suitable cluster in an N-body simulation of a large region that contains many clusters; then we resimulate the cluster and its immediate environment at higher resolution. In this case, the original low-resolution simulation we chose was one of those described by Frenk et al. (1990). It used 262,144 particles to follow the evolution of the dark matter distribution in a box 360 Mpc on a side, assuming standard CDM initial conditions ($\Omega = 1$, $h = 0.5$, and normalization at 8 h^{-1} Mpc, $\sigma_8 = 0.59$). The chosen cluster had a one-dimensional velocity dispersion of $\sim$1000 km s^{-1} and a "turnaround radius" of $\sim$10 Mpc.

We replicated the initial displacements due to longer wavelength modes ($\lambda > 11.25$ Mpc) in this low-resolution simulation on a 128^3 cubic grid of side 45 Mpc centered on the barycenter of the cluster material. After subtracting the mean of this displacement field, we apodized it with a cosine bell in order to avoid finite displacements at the edge of the box. This apodization modifies the initial displacements within 1.5 comoving Mpc of the boundary. Everywhere interior to the apodized region the displacement field has the same divergence, and thus it corresponds to the same linear overdensity field, as was produced by the long-wavelength modes in the original simulation. To this low-frequency displacement field we added random phase contributions (assumed periodic on the 45 Mpc box) of the amplitude predicted by our CDM spectrum. The combined displacement field was then used to move 64^3 dark matter particles from a cubic grid. This gives initial positions for the simulation of cluster evolution within a 45 Mpc box with periodic boundary conditions. Initial velocities were set according to linear theory in proportion to the forces generated by this particle distribution.

The resulting initial conditions have a mass resolution about 500 times better than the original simulation. Everywhere out to about twice the final turnround radius of the cluster, the large-scale *linear* density evolution is identical to that in the original model. The large-scale *nonlinear* evolution might differ if it is influenced strongly by tidal forces from matter more than 25 Mpc from cluster center. We do not expect such effects to be large in comparison to the scatter between different clusters in a CDM universe and, in any case, we are more interested in small-scale processes occurring within the cluster than in its large-scale morphology and environment. In fact, the cluster we describe below has a turnround radius and a density profile that agree quite well with those of the original cluster (although the latter has only about 200 particles and so results are quite noisy). In addition, both the evolution and the final structure of our cluster are similar to those of the "typical" CDM clusters simulated at lower resolution by Navarro et al. (1995). Thus, we are confident that our procedure for simulating the formation of a Coma-like cluster within a periodic box of side "only" 45 Mpc has not introduced any artifacts that affect significantly our conclusions.

Ten percent of the mass of each dark mass particle was removed and assigned to a gas particle with identical position and velocity and a temperature of 10^4 K. Thus, we are assuming $\Omega_b = 0.1$. We use a fixed comoving gravitational softening parameter $\epsilon = 35$ kpc in the Plummer potential, $\phi(r) \sim (r^2 + \epsilon^2)^{-1/2}$. Within P3MSPH, the SPH smoothing parameter, h, is never allowed to fall below 0.5ϵ; its upper limit is set by the size of the P^{3}M chaining mesh. This results in an effective spatial resolution in the densest regions of $\simeq 2\epsilon$. We follow evolution from redshift $z_i = 12.4$ to the present using 700 equally spaced time steps.

2.2. *Resolution Effects*

Our first experiment failed to produce an appreciable number of galaxies. By redshift $z = 0.18$, when the simulation was stopped, gas had been able to cool onto only four distinct objects containing 32 or more particles and with density contrast $\sim 10^6$. We interpret this problem as resulting from inadequate mass resolution. Each of our gas particles has a mass of $2.4 \times 10^9\ M_\odot$. This is a factor 24 larger than the corresponding mass in the experiment of ESD and a factor of 2 larger than that in the model of Katz et al. (1992). An L_* galaxy would thus correspond to a clump of about 40 gas particles, right at the resolution limit of the experiment. Real clusters of this mass contain roughly 50 L_* galaxies, and analytic work by Kauffmann, White, & Guiderdoni (1993) shows that the kind of CDM model we are studying should produce approximately the right number of such galaxies. It appears that the smoothing required to estimate densities for our SPH particles leads to these densities being substantially underestimated, and to cooling times being substantially overestimated, in the clumps of gas and dark matter that correspond to the halos of L_* galaxies.

To check this hypothesis, we ran a second simulation using the same initial displacements and velocities, but with an altered cooling law. We calculated a cooling time for each particle [$t_c = T/(dT/dt)$] using the SPH density estimate but a temperature and internal energy 4 times smaller than the SPH values. This results in a substantial increase in cooling efficiency when the true temperature is of order 10^6 K, the value expected within halos of large galaxies. In the absence of radiative cooling, the evolution of the two simulations would, of course, be identical. However, while cooling had little effect on the first simulation, the second (hereafter referred to as the "gas" simulation) produced a few hundred dense, cold objects of galactic mass (the "globs" of ESD). This test confirms that the lack of galaxies in the first model is indeed a result of inefficient cooling rather than of any inability to treat protogalactic collapse in our SPH scheme. Figure 1 below shows that objects made up of a few tens of particles are significantly less concentrated in the gas component than in the dark matter, whereas studies of individual objects carried out with much higher resolution suggest that the gas should, if anything, be more concentrated. This explains why cooling times are overestimated if no ad hoc alteration of the cooling law is made to compensate. Of course, the alteration we have made is very crude, but it is adequate to produce a population of objects whose later dynamical evolution we can

follow. Qualitatively, this modification has a similar effect to that of a cooling function in which metal line cooling is included.

2.3. *Dynamical Treatment of the Galaxy Population*

One of the main aims of this paper is to investigate the consequences of the inevitable assumptions and simplifications needed to model realistic clusters with simulations. Real galaxies are, of course, made predominantly of stars rather than cold gas. Therefore, we designed an experiment to test the dynamical consequences of neglecting star formation. At a redshift of 0.7, well before the collapse of the main cluster but well after a significant amount of gas has condensed into cool clumps, we identified candidate galaxies by using a friends-of-friends grouping algorithm on the gas particles (Davis et al. 1985). We adopted a linking length that was only 1.7% of the mean interparticle separation and so identified objects at very high density contrast ($\sim 10^5$). All the gas particles in groups with 32 or more members were converted instantaneously into collisionless "star" particles. All the remaining gas was removed and the mass associated with it was distributed uniformly among nearby dark matter particles. The resulting distribution of "stars" and dark matter was evolved from $z = 0.7$ to $z = 0$ with a collisionless P^3M code. We will refer to this calculation as the "star" simulation and to collapsed objects containing stars as "S-gals" to distinguish them from the purely gaseous objects in the original simulation, which we refer to as "G-gals."

3. GALAXY AND CLUSTER FORMATION

Figure 1 shows the distribution of dark matter (*left*) and gas (*right*) in a slice with sides one-half and thickness one-tenth that of the total volume in the "gas" simulation. Three different epochs are shown, corresponding to redshifts $z = 2$, 0.7, and 0. Both the dark matter and the gas fall coherently onto the central density enhancement. The flow is highly inhomogenous, and a complex filamentary pattern, converging at the centre, is clearly visible. In spite of these high contrast features, the flow is never highly anisotropic: as we shall see below, the particles that end up in the cluster come from a roughly spherical initial region. At $z = 0.7$, several large subcondensations have formed. These all merge by $z = 0$, but even then the cluster does not yet appear fully relaxed. As the large subclumps come together, their dark matter interpenetrates, but their gas is shocked. Energy is transferred during the collision, both from the dark matter to the hot gas (Navarro & White 1994; Pearce, Thomas, & Couchman 1994) and from the cold to hot phases of the gas itself due to viscous braking of infalling G-gals. As a result, the hot gas ends up being somewhat more extended than the dark matter. Because of its (isotropic) pressure support, the gas also has a rounder configuration. Notice that the dense clumps of cold gas, while present, are not readily visible in Figure 1 due to their extremely small volume filling factor.

3.1. *The Assembly of the Cluster Material*

Our working definition of the cluster is the material within a sphere of radius 4 Mpc centered on the largest dark matter clump at $z = 0$. The mean mass density contrast within this sphere is ~ 110. Although this is slightly larger than the fiducial cluster radius (within which $\delta\rho/\rho = 180$), we shall see in § 4 below that some material that has passed through the cluster center lies beyond 4 Mpc.

Figure 2 illustrates the time evolution of the material that ends up in the body of the cluster. Distributions of dark matter, hot gas ($T > 1.2 \times 10^7$ K), cool gas ($T < 1.2 \times 10^7$ K), G-gals, and S-gals are plotted. Time runs from left to right, and the six epochs shown correspond to redshifts $z = 2$, 1, 0.7, 0.3, 0.1, and 0 respectively. The cluster is assembled in a very lumpy fashion. The large subcondensations seen at early times in Figure 1 fall together and are disrupted between $z = 0.3$ and $z = 0.1$, producing a diffuse dark matter background containing smaller, high-contrast lumps. By $z = 0.1$, most of the large lumps have disappeared, but a few smaller dark matter halos still survive. By $z = 0$, the dark matter distribution is smooth and centrally concentrated, and most of the remaining galactic halos lie in the periphery of the cluster.

At early times, the gas is (by assumption) cold, and so it clusters with the dark matter. As soon as dark matter halos form that are sufficiently large to be resolved by the SPH technique, their associated gas falls to halo center, where it settles into a cold, centrifugally supported disk (ESD). During such collapses, some of the gas is shock heated to form smooth hot coronae. The largest of these (those associated with dark matter clumps with virial temperatures above 1.2×10^7 K) may be seen in Figure 2*b*. As the cluster grows, an increasing fraction of the cold gas collects in small nonlinear clumps, but much of the gas remains diffuse or in hot coronae, and these components merge until, by the present day, most of the gas in the cluster is in a hot rarefied atmosphere near hydrostatic equilibrium and with no appreciable substructure.

The first G-gals form before $z = 2$, and their abundance grows rapidly so that by $z = 0.7$, when large precluster condensations are collapsing, there is already a sizable population of them. It is at this time that we turn G-gals into S-gals in the "star run." The subsequent evolution of the galaxy populations in the two runs is rather different. The G-gals experience viscous interactions, and their collisions are sticky. As a result, they tend to merge into a single massive object at the center of the cluster, which eventually contains almost half the cold gas in the cluster. Occasionally G-gals are removed from their halos and disrupted as they fall through the hot gas. An example of this process can be seen near the top left-hand corner of the $z = 0$ panel of Figure 2*c*.

Further details of the evolution of the hot gas are illustrated in Figure 3. The first three columns show contour diagrams of the projected dark matter distribution, gas density, and gas temperature within a physical region of size 6.6 Mpc. The epochs shown correspond to redshifts of 0.7, 0.3, 0.1, and 0.03. Qualitatively, the evolution of the gas distribution resembles that of the dark matter, but shocks lead to transient features in the gas that are visible in the density and temperature plots. Note how the gas is compressed and heated at the interface of the two large merging subunits at $z = 0.3$, producing a stream of hot, diffuse gas that squirts in the direction perpendicular to the axis of the collision. At $z = 0$, the gas near the center remains quite inhomogeneous as it cools and sloshes around in the varying gravitational potential. The rapid decline in the population of small dark matter halos is seen easily in the projected mass distribution. Note that by $z = 0.03$ very few such halos remain, most of those in the outskirts of the

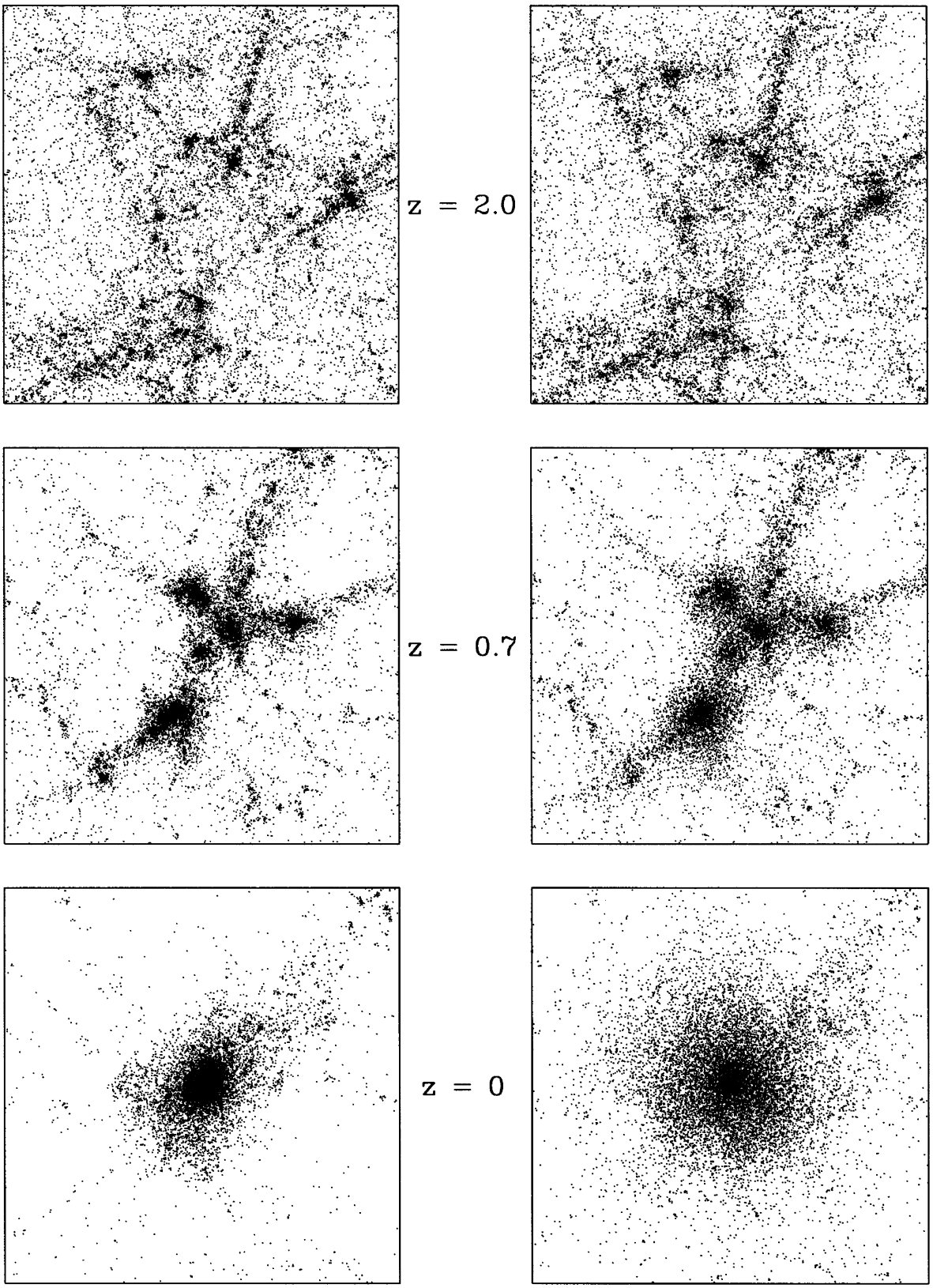

FIG. 1.—The distribution of a random subset of dark matter particles (*left*) and gas particles (*right*) at redshifts $z = 2$ (*top*), $z = 0.7$ (*middle*), and $z = 0$ (*bottom*) located in a comoving square slice half the size of the simulation volume. The slice thickness is 4.5 (physical) Mpc.

cluster. The largest G-gals show up in the density and temperature plots as dense condensations of low-entropy gas. Small galaxies are not resolved in this projected image.

The last column in Figure 3 shows contour maps of X-ray luminosity in the *ROSAT* passband (0.5–2.4 keV) obtained from the density and temperature of the gas in the manner described by Evrard (1990). These X-ray images are what a hypothetical satellite would see if situated a fixed distance of 180 Mpc (corresponding to an effective source—observer redshift of 0.03) from the cluster at all epochs. These X-ray

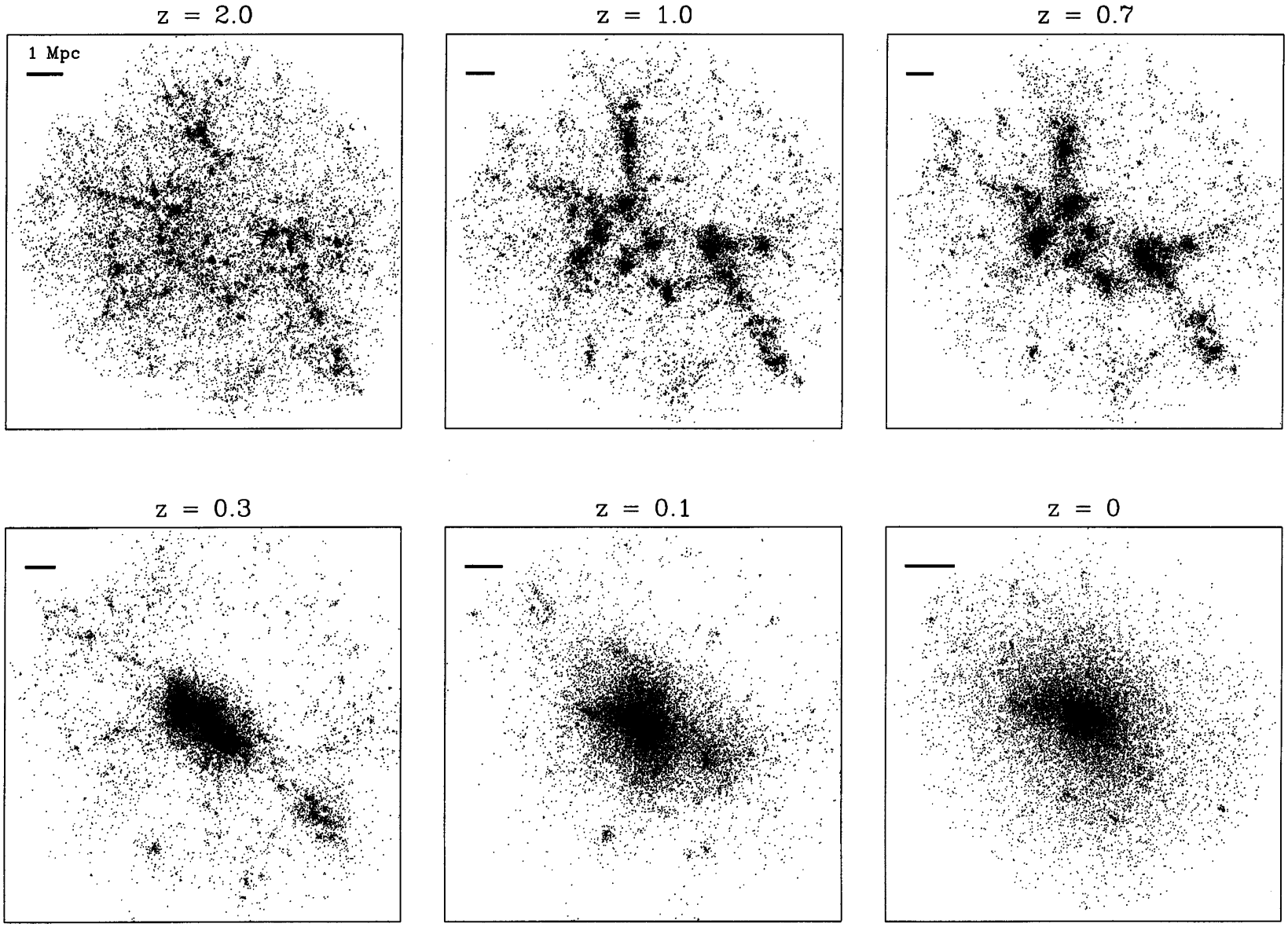

FIG. 2*a*

FIG. 2.—Evolution of the cluster components: (*a*) dark matter; (*b*) hot gas ($T > 1.2 \times 10^7$ K); (*c*) cold gas ($T < 1.2 \times 10^7$ K); (*d*) G-gals; (*e*) S-gals; and (*f*) dark matter halos. The different panels show the positions of those particles which, at $z = 0$, are contained within a sphere of radius 4 Mpc centered on the cluster. Redshifts are labeled on each panel. A random subset of particles is shown for each component. The definition and properties of the dark matter halos are discussed in § 3.2.

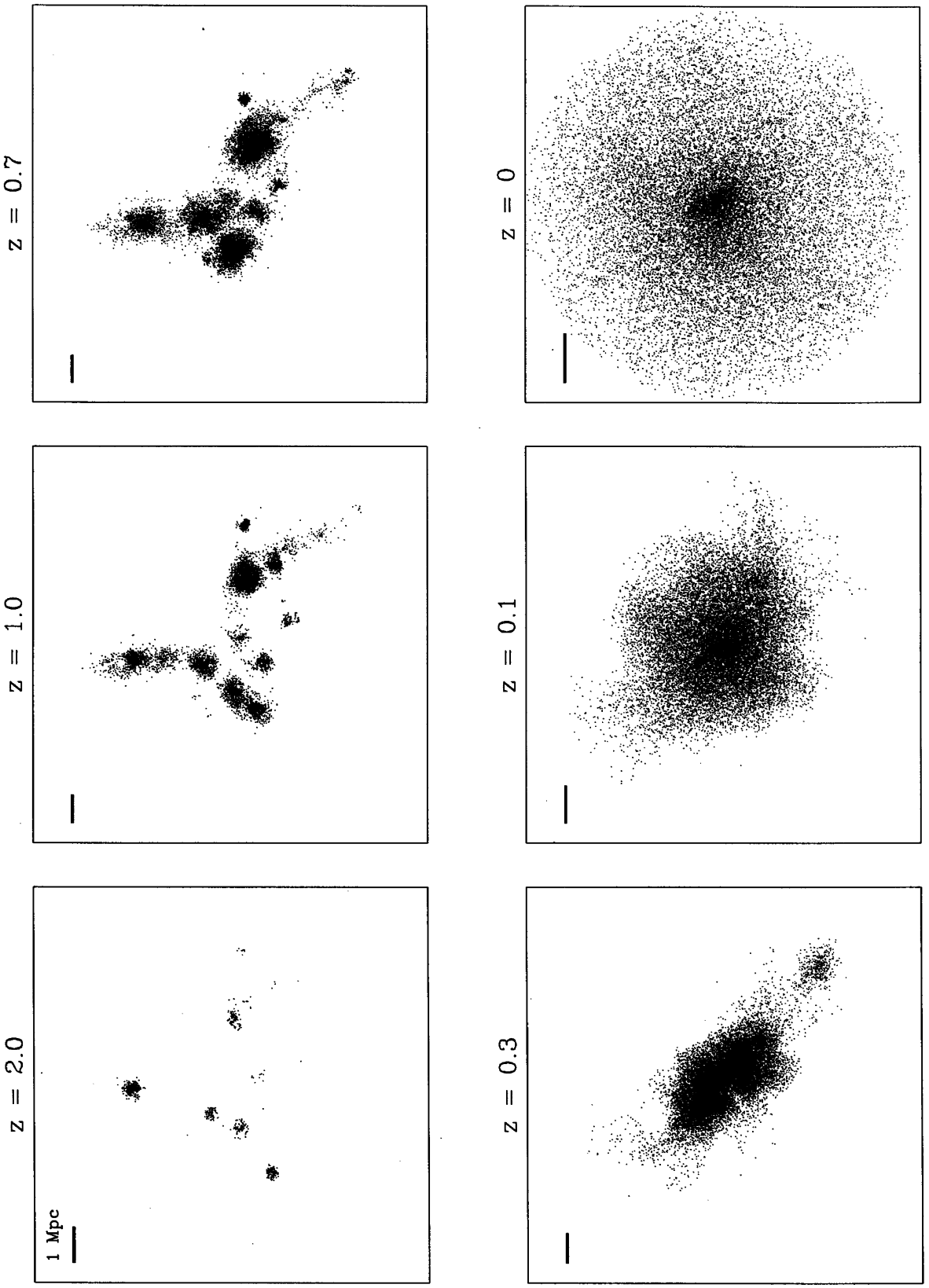

FIG. 2*b*

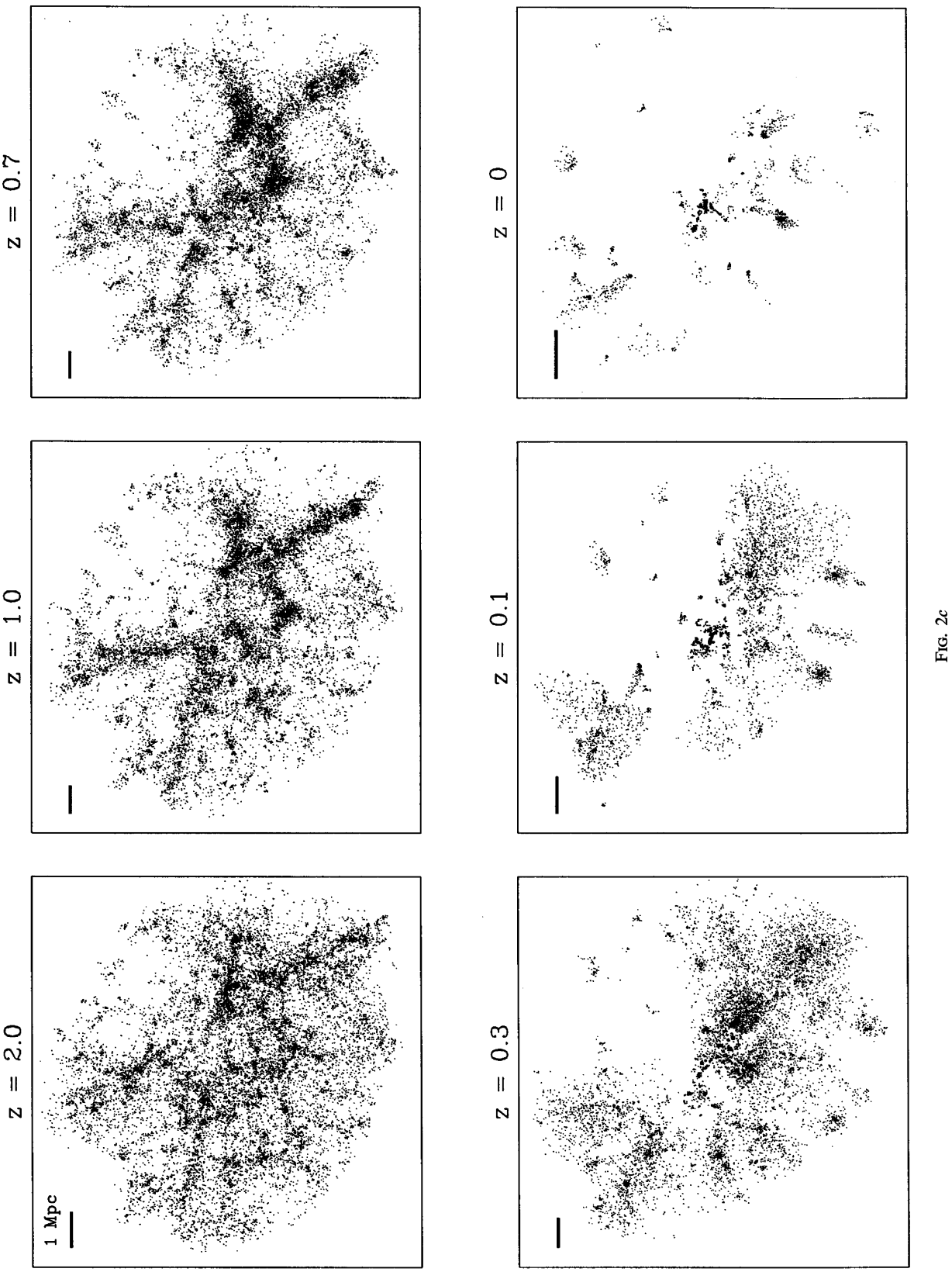

FIG. 2*c*

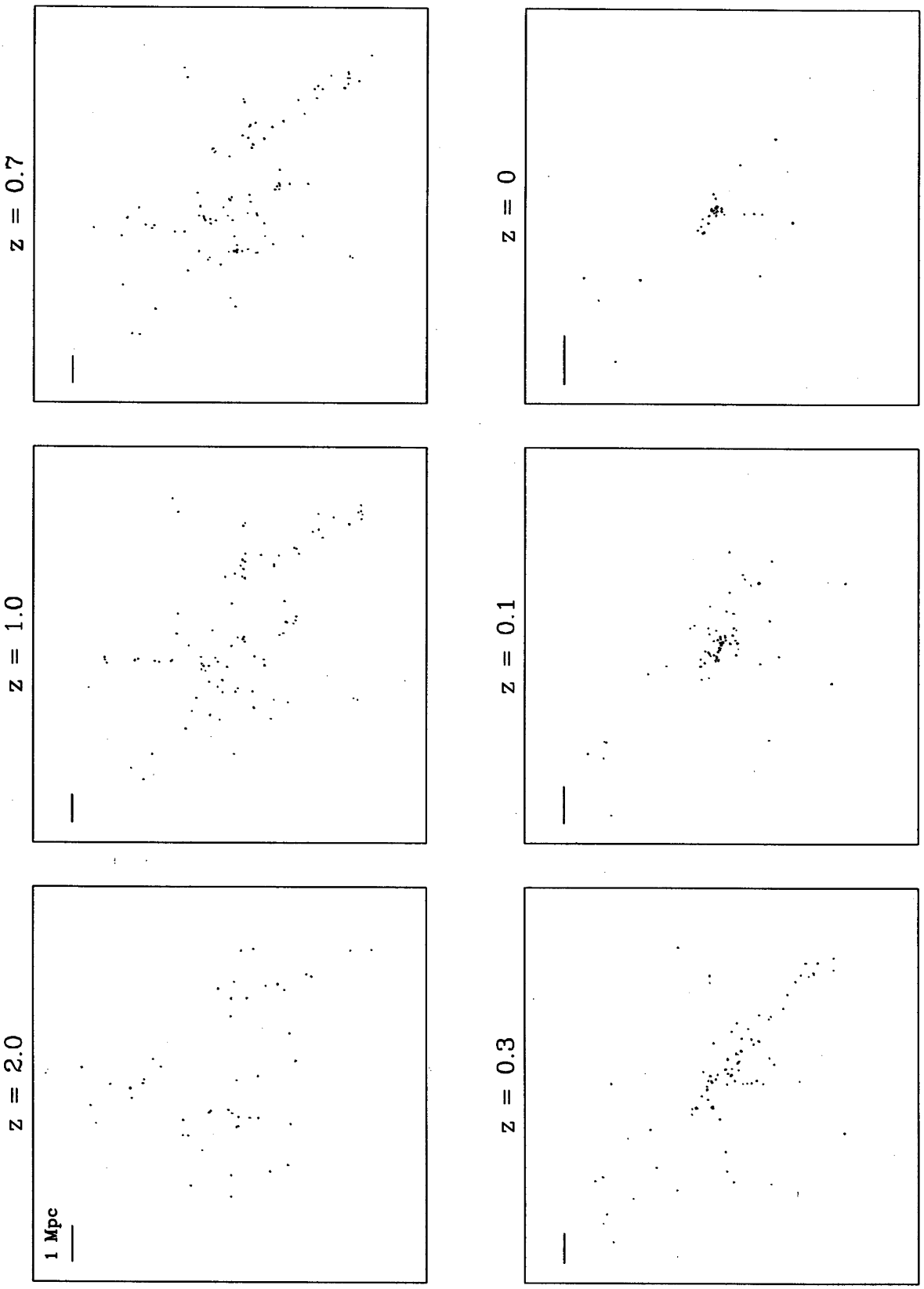

FIG. 2*d*

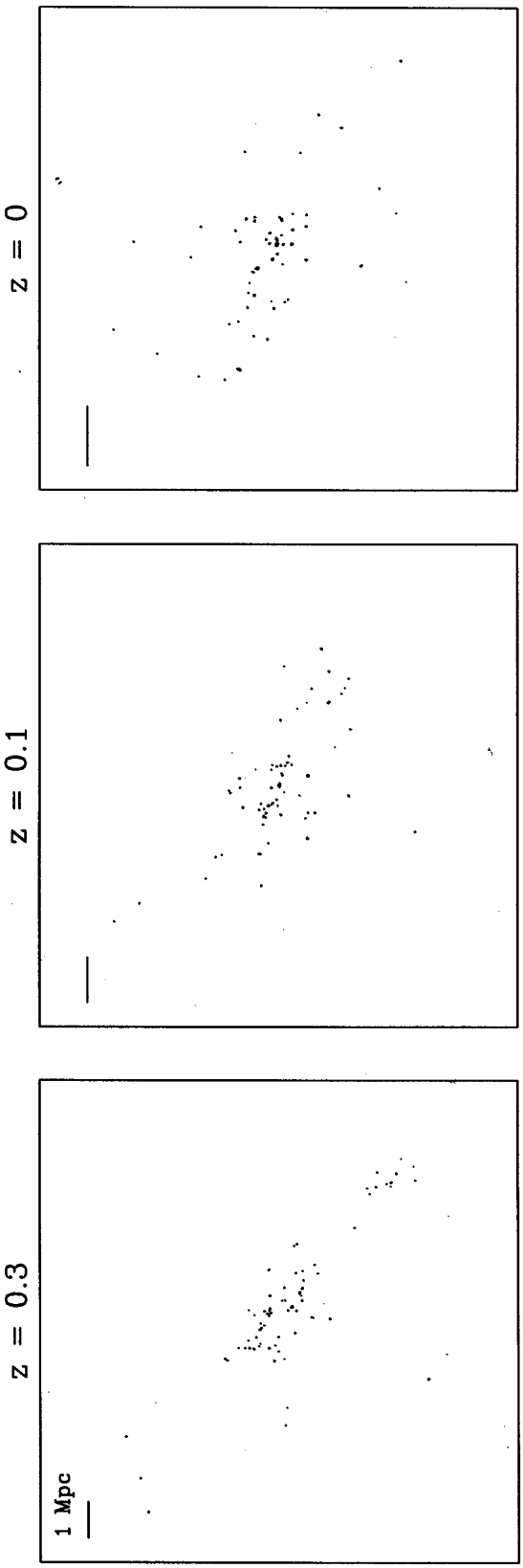

FIG. 2*e*

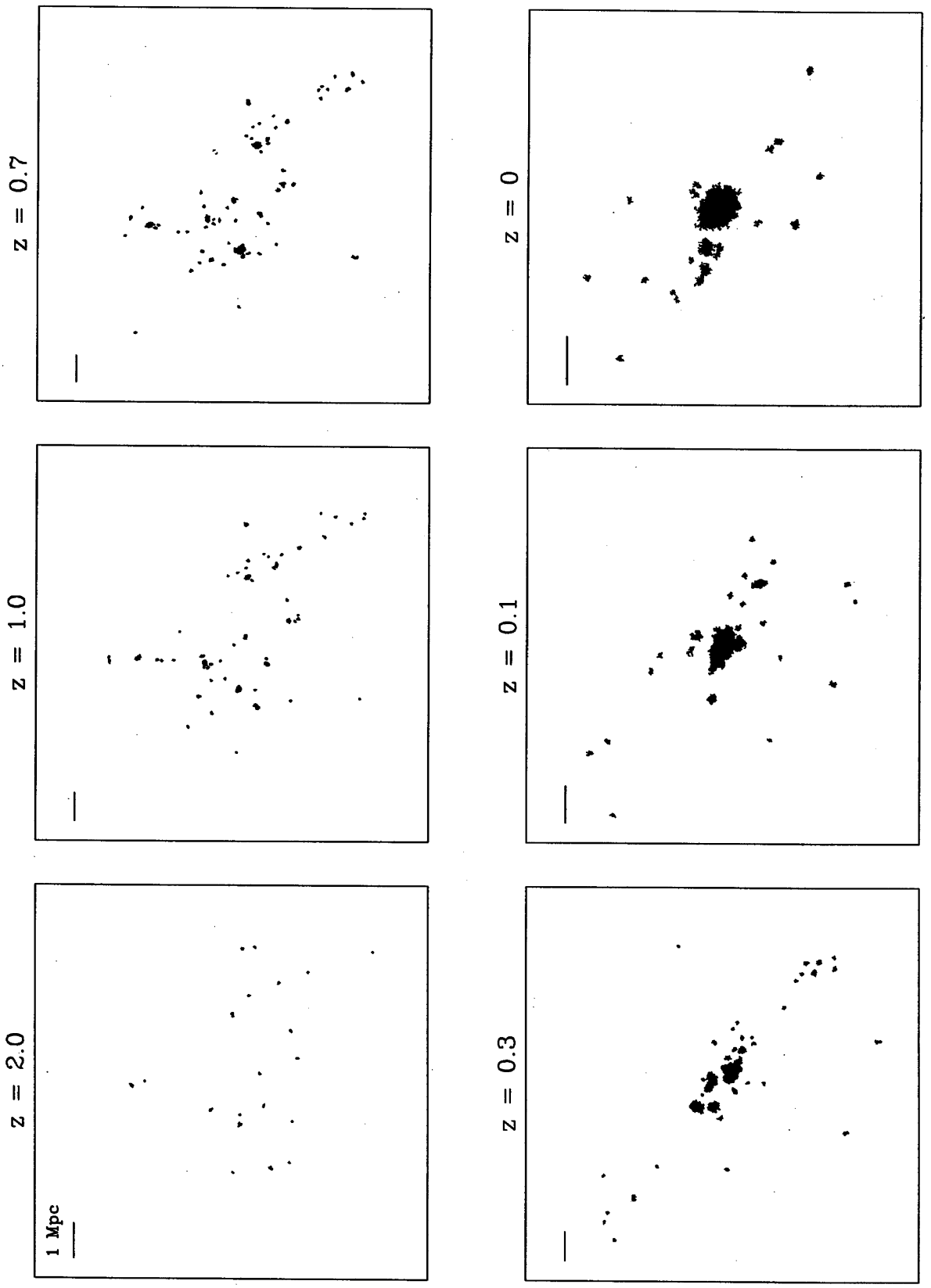

FIG. 2*f*

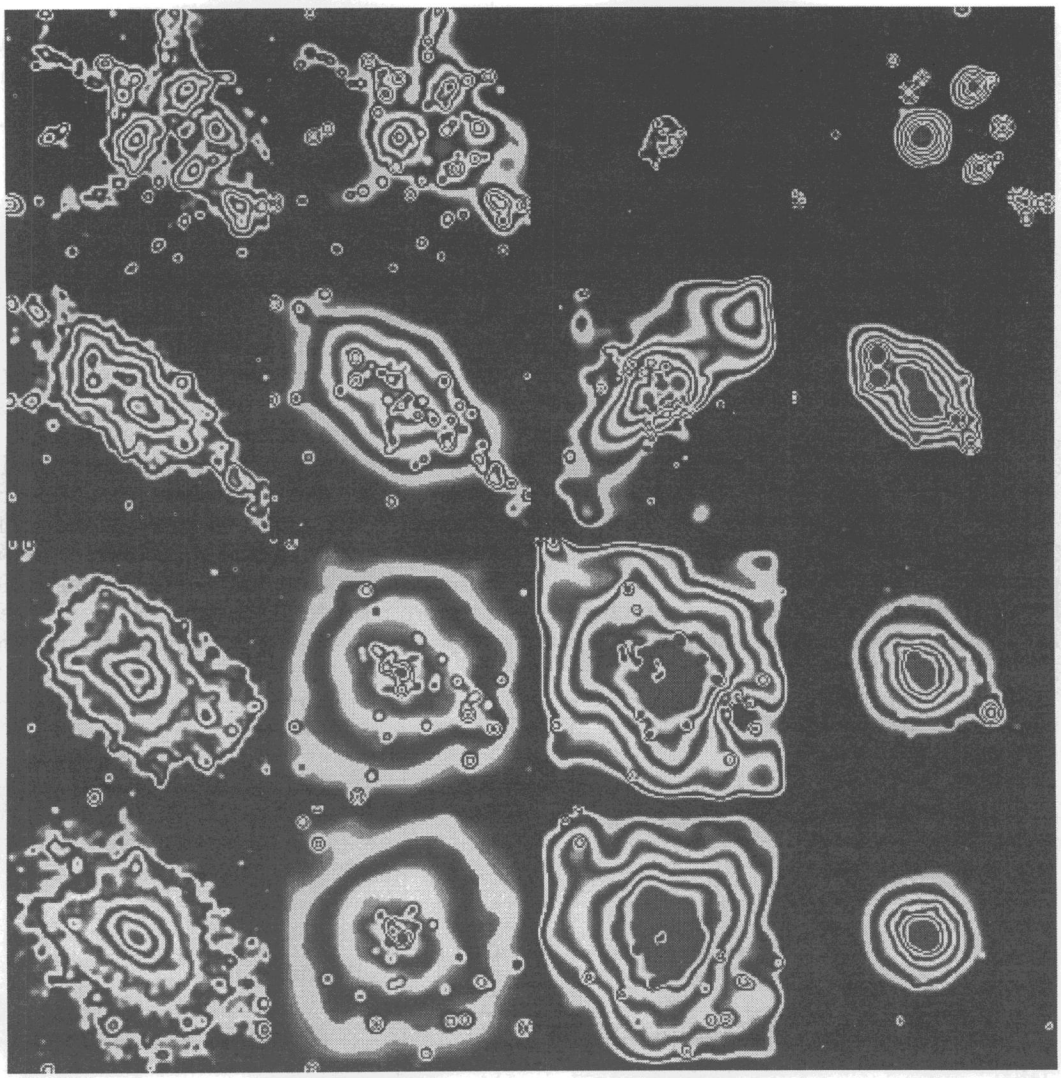

FIG. 3.—Gray-scale maps of, from left to right, the projected dark matter density, projected baryon density, emission-weighted temperature, and *ROSAT* X-ray surface brightness. The maps are generated by placing the cluster at an effective redshift of 0.03 (180 Mpc) from the hypothetical observer. The angular size of the region is 128′, and the angular resolution is a minimum of 1′. From top to bottom, the epochs shown correspond to redshifts $z = 0.7$, 0.3, 0.1, and 0.03, respectively. The spacing between light or dark bands is approximately a factor of 2, except for the temperature maps, where the spacing is ~25%.

images illustrate clearly the dynamically complex nature of cluster formation. At $z = 0.7$, the cluster is broken up into several distinct subunits with a wide range of sizes. Cooling is important in the smaller knots, which appear more centrally concentrated than the two dominant components. A few tightly bound subunits of high surface brightness survive at $z = 0.3$, when the central region of the cluster shows a clear double structure. By $z = 0.1$, the X-ray isophotes are still irregular and have the "boxy" appearance characteristic of a major ongoing merger. A bright subclump infalls into the central regions from the lower right. Note the factor of ~2 drop in the projected temperature map across the interface between the main body of the cluster and the subclump. By $z = 0.03$, this subclump has merged with the main cluster, and the X-ray appearance of the cluster is fairly regular, with outer isophotes somewhat elongated along the principal collision axis. At $z = 0.03$, the total X-ray luminosity (in the *ROSAT* band) emitted by the region shown is 4.9×10^{44} ergs s^{-1}.

3.2. *The Abundance of Galaxies and Dark Halos*

In this section, we quantify the abundance of galaxies in our simulations and investigate how it is affected by the cluster environment. At each epoch, we identify G-gals or S-gals using a friends-of-friends group finder (Davis et al. 1985) on the appropriate particle distribution, with a linking length of $\eta = 0.01(1 + z)$ of the mean interparticle separation. This procedure picks out regions that lie above a fixed *physical* density threshold of roughly 0.5 cm^{-3}. The procedure is identical to that used by ESD. We also examine dark matter halos, but we identify them in a slightly different manner. Lacking dissipation, the dark matter does not achieve the high density contrasts seen in the baryons, and so we identify dark halos with a redshift-independent linking length equal to 5% of the mean interparticle separation. This value picks out objects at a fixed density contrast of roughly 8000. The distribution of G-gals, S-gals, and dark matter halos at various redshifts is shown in Figure 2.

Note that the number of dark matter halos associated with the cluster is quite sensitive to the choice of linking parameter, but the number of G- and S-gals is not. Because of the two-phase structure of the baryonic gas, the G-gals and S-gals all have very high density contrast and are picked out easily by the group finder. The dissipationless nature of the dark matter, on the other hand, results in a

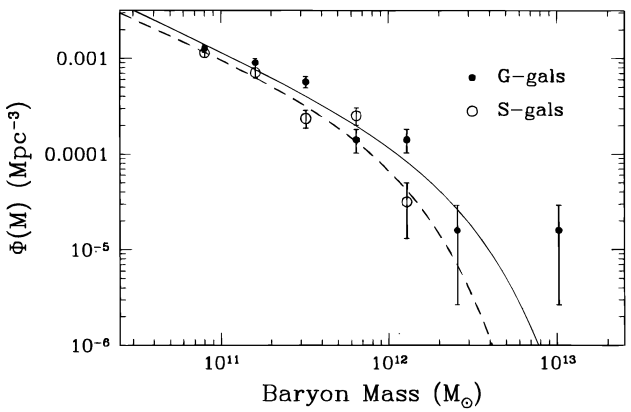

FIG. 4.—Differential mass functions of galaxies in the entire volume. The best-fitting Schechter functions are shown for the G-gals (*solid line*) and S-gals (*dashed line*).

(comparatively) smoother density field in collapsed structures, leading to a continuously varying population of halos as a function of η. For the simulation as a whole, our choice of $\eta = 0.05$ yields a mass fraction in dark halos with 32 or more particles that is similar to the fraction of the gas in the form of G-gals.

TABLE 1

LARGEST CLUSTER MEMBERS

Type	M_1	M_2	M_3
DM halos.....	14,988	440	223
G-gals	5062	1612	664
S-gals.....	728	552	500

At the final time in the simulation, 12% of the total gas mass in the "gas" simulation resides in G-gals, whereas only 6% of the gas mass in the "star" simulation ends up in S-gals. This difference is due primarily to the rise in the G-gal population due to continued cooling of gas into newly formed dark matter halos. By contrast, the population of S-gals cannot increase after its formation but it can decline by merging and tidal disruption. At $z = 0$, in the entire volume there are 195 G-gals and 150 S-gals with 32 or more particles (i.e., with "baryonic" mass greater than $7.7 \times 10^{10}\ M_\odot$). The corresponding numbers in the cluster

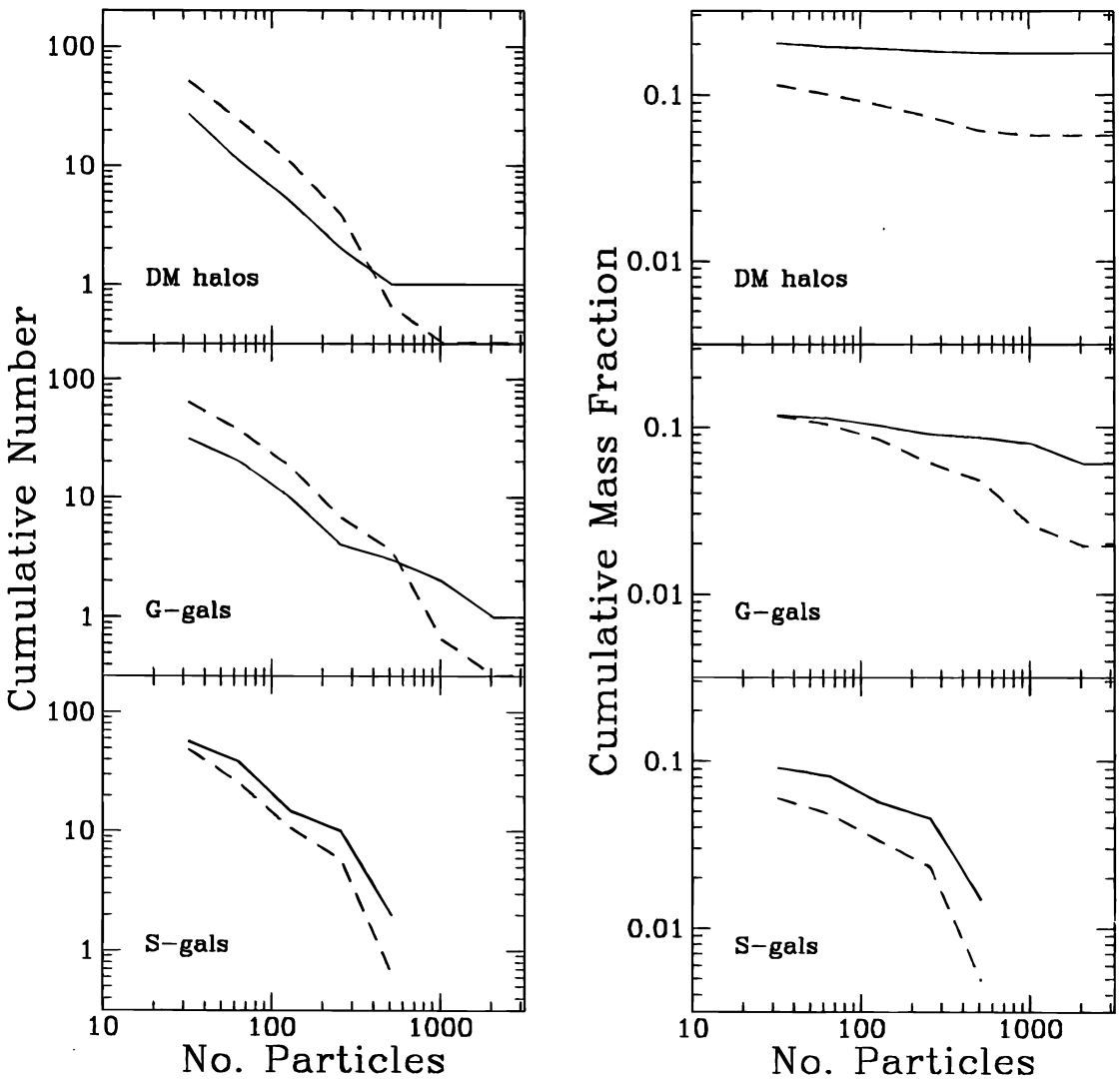

FIG. 5.—Cumulative multiplicity functions of objects in the cluster (*solid lines*) compared to predictions based on data from the entire volume (*dashed lines*). *Left:* The number of objects of each multiplicity. *Right:* The mass fraction represented by each type of object. In the cluster, the mass fraction is normalized to the number of dark matter particles in the cluster and, in the entire volume, to the total number of dark matter particles. The S-gals are the only population that is overrepresented ("positively biased") within the cluster in both number and mass-weighted senses.

region, within the fiducal radius of 4 Mpc, are 31 G-gals and 59 S-gals. Thus, the fractional abundance of S-gals in the clusters exceeds that of the G-gals by a factor 2.5, reflecting primarily the higher merger rate of G-gals relative to S-gals in the cluster.

The number of dark matter halos with 32 or more particles (i.e., with mass greater than $6.9 \times 10^{11}\ M_\odot$) in the entire volume is comparable to the number of S-gals but, in the cluster, only 27 dark halos survive at the end, most of them in the cluster periphery. About one-third of the dark matter particles (85,018 in the gas run and 83,836 in the star run) end up in the cluster region.

The present-day differential mass functions for G-gals and S-gals within the entire volume are displayed in Figure 4. Except at the very massive end, the G-gal and S-gal mass distributions are quite similar. Both are moderately well fit by the Schechter function, which is often used to describe the observed luminosity function of galaxies,

$$\Phi(L/L_*)dL/L_* = \Phi_*(L/L_*)^\alpha \exp - (L/L_*)\ dL/L_* . \quad (1)$$

The slope at the low-mass end is $\alpha \simeq -1.8$. Such a steep slope is a well-known feature of hierarchical clustering models of the kind assumed here. It has been noted before both in analytic work (White & Rees 1978; White & Frenk 1991; Cole 1991) and in numerical simulations (ESD). It is considerably steeper than the faint-end slope of the field galaxy luminosity function, $\alpha \simeq -1$, measured by Loveday et al. 1992 (but compare Marzke, Huchra, & Geller 1994).

The mass functions of objects in the cluster are noiser than those in the entire volume, and so we show them in cumulative form in Figure 5. The left panels show distributions by number, whereas the right panels show mass-weighted distributions, normalized by the number, $N_{\rm DM}$, of dark matter particles within the cluster. In both panels, the solid lines show the actual cluster distributions, while the dashed lines show the corresponding distributions in the entire volume, multiplied by the factor $N_{\rm DM}/64^3$. If the cluster populations were typical of those in the field, the solid and dashed lines in Figure 5 would coincide. Instead, we see that there are significant biases in the populations of all types of collapsed objects in the cluster.

In a number-weighted sense, both dark matter halos and G-gals are negatively biased in the cluster except at the high-mass end, where the single most massive, central object dominates. This is particularly true for the dark matter halo population; the central object contains over 80% of the mass in halos in the cluster. For the G-gals, the number bias is positive only for objects with more than $\sim$550 particles, corresponding to a baryon mass of $1.3 \times 10^{12}\ M_\odot$. The degree to which the most massive object dominates is exhibited in Table 1, which lists the masses of the top three objects of each type found in the cluster at $z = 0$. For the dark matter halos, the ratio of the first to second ranked objects is $M_1/M_2 = 34.1$. The G-gals are also top-heavy, but with a much smaller value of $M_1/M_2 = 3.14$. The S-gals are relatively well balanced, with $M_1/M_2 = 1.32$.

In a mass-weighted sense, both dark halos and G-gals are positively biased in the cluster. The S-gals are the only population that is positively biased in both number- and mass-weighted senses over all mass ranges resolved. These biases are all mass dependent. For example, S-gals with 32 or more particles are biased by a factor of $\sim$1.6, but S-gals with 512 or more particles are biased by a factor of 3.1, the maximum allowed when all objects of a given type are found exclusively in the cluster.

4. CLUSTER STRUCTURE AND DYNAMICS

In this section we investigate the structure and dynamical properties of our model clusters. We examine the spatial distribution of the various components, their orbits, merger histories, and binding energies. We also carry out a virial analysis similar to those used to estimate the mass of real galaxy clusters and, hence, the value of the mean cosmological density, Ω.

4.1. *Spatial Distributions of Dark Matter, Hot Gas, and Galaxies*

It is apparent from the previous section that the final spatial distributions of the various constituents of the cluster—dark matter, hot gas, dark matter halos, G-gals, and S-gals—differ to varying degrees. This impression is quantified in Figure 6, which shows the comulative mass or number density profiles of the components. The center of the cluster is taken to be at the position of minimum binding energy, and the profiles are plotted in terms of the radius normalized to our fiducial cluster value $r_{\rm cl} = 4$ Mpc. Note that the "virial radius," conventionally defined by the sphere that encompasses a mean overdensity of 180, is $r_{\rm vir} = 3.4$ Mpc.

The dark matter profiles from both the gas and star runs are shown in the top panel of Figure 6; the former is slightly more concentrated due to the influence of the central, dominant G-gal. The profiles bend continuously from the center outward. The spherically averaged, differential density profile of the dark matter from the star run is shown in Figure 7. It is well fitted by the function

$$\frac{\rho_{\rm DM}}{\bar\rho} = \frac{1500\ r_{\rm vir}^3}{r\ (5r + r_{\rm vir})^2}\ , \quad (2)$$

where $\bar\rho$ is the mean density of the universe and $r_{\rm vir}$ is the virial radius defined above. This is the same function that fits the scaled dark matter profiles of the clusters in the simulations of Navarro et al. (1995), but the present simulation has over 20 times more particles and thus resolves the central regions considerably better. To our resolution limit, there is no evidence for a central core radius. Instead, the density continues to increase toward the center, roughly as $\rho_{\rm DM} \propto r^{-1}$ [corresponding to $M(r) \propto r^2$]. In the range $0.1 \lesssim r/r_{\rm vir} \lesssim 0.4$, it flattens to an approximate isothermal form, $\rho_{\rm DM} \propto r^{-2}$ and, beyond that, it falls off more steeply, approximately as $\rho_{\rm DM} \propto r^{-2.4}$. In the inner parts, this behavior is similar to that found by Dubinski & Carlberg (1991). The excellent agreement between the cluster dark matter profile in this simulation and those obtained by Navarro et al. (1995) is evidence that our simulation procedure (which ignores tidal effects beyond the simulated volume) has not introduced significant systematic errors into our calculation.

The hot, intracluster gas follows a nearly power-law profile, with slope -2.2, over the entire range plotted, $\sim$0.14 Mpc to 4 Mpc. The profile actually steepens in the center, and the resulting X-ray surface brightness profile resembles that of a cluster with a strong cooling flow. The hot phase is more extended than the dark matter, with a half-mass radius (defined within $r_{\rm cl}$) nearly a factor 2 larger.

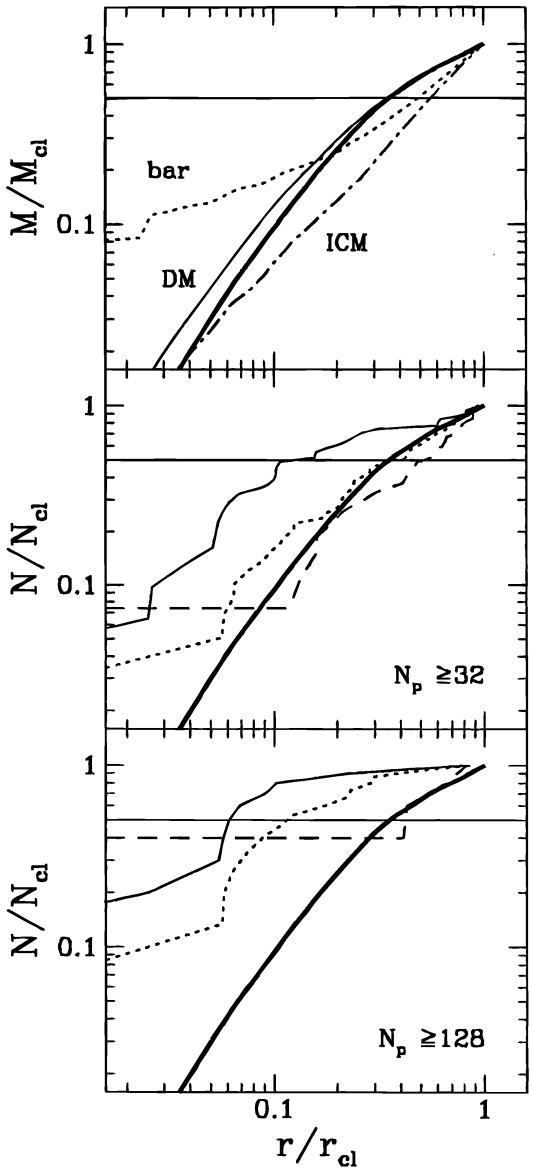

FIG. 6.—Normalized cumulative profiles in the final cluster. *Top:* The dark matter mass profile in the star run (*thick solid line*) and gas run (*thin solid line*) as well as the enclosed total baryon (*dotted line*) and hot gas (*dot-dashed line*) mass profiles. *Middle and bottom:* The normalized enclosed number profiles, for two mass ranges, for the G-gals (*solid line*), S-gals (*dotted line*), and dark matter halos (*dashed line*) compared with the enclosed mass profile of the dark matter from the star run (*thick solid line*).

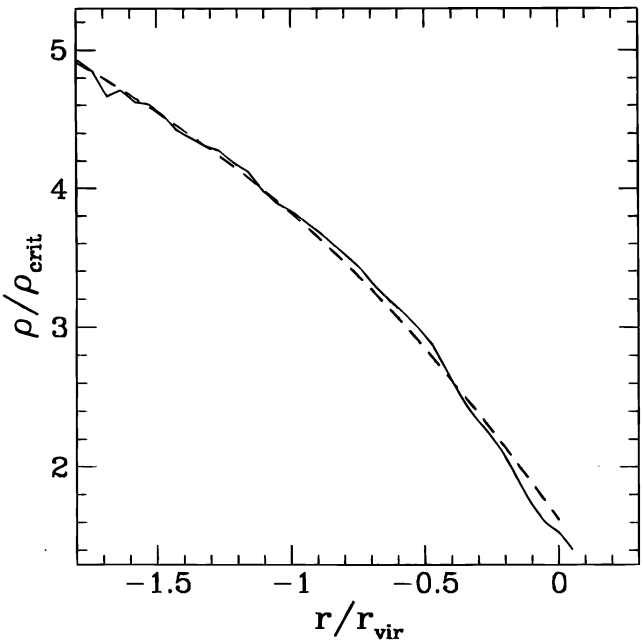

FIG. 7.—Differential density profile of the dark matter in the cluster. The solid line shows the profile in the star run, and the dashed line shows the fitting formula from Navarro et al. (1995), eq. (4).

The more extended distribution of the hot gas reflects transfer of energy from the dark matter (Navarro & White 1994; Pearce et al. 1994) and cold gas and transfer of material to the cold phase. The total baryon fraction is dominated by hot gas in the outer parts of the cluster and by cold, G-gal material in the inner few hundred kiloparsecs. Within 4 Mpc of the cluster center, the mean baryon fraction in the gas run is 0.075, smaller than the global value by 25%.

The cumulative number distributions of dark matter halos, G-gals, and S-gals in two different mass ranges are shown in the bottom two panels of Figure 6. The dark matter halos are the most extended component, primarily because of the presence of the massive, central halo; in essence, the cluster itself. The S-gals ($N \geq 32$) are more concentrated than the dark mass in the inner regions but, beyond $\simeq 0.2 r_{cl}$, they trace closely the dark matter. The G-gals are highly concentrated, with a half-number radius nearly a factor of 3 smaller than the half-mass radius of the dark matter. Galaxies of both types exhibit mass segregation, with more massive objects being more centrally condensed. This is a weaker effect for the S-gals. The outer slope of the S-gal number density profile is -2.3, slightly shallower than the profiles typically observed for galaxies in real clusters (e.g., Schombert 1988).

4.2. *Galactic Orbits and Merger History*

In an effort to understand the origin of the differences between the final cluster G- and S-gal populations, we examine their orbits and merger histories. Orbits of the 16 most massive cluster G- and S-gals are plotted in Figure 8. To trace the orbits, the membership list of groups at successive outputs are compared, and a group at the later time is identified with one at the earlier time if more than half the latter's members are included in the former. The time interval between outputs is approximately 2×10^8 yr. The positions of the center of mass are plotted as dots in the figure; the cross marks the position of the center of the cluster at $z = 0$. The number in each panel gives the mass rank of the object at $z = 0.7$. Gaps in the ranks arise from objects that lie outside the body of the cluster. Notice that several of the orbits plotted are identical at later times as a result of merging of the objects considered.

The degree of difference in the orbits of the G-gals and S-gals depends on mass. Both types of objects have predominantly radial orbits, exaggerated in the figure by the use of comoving positions. The infall portions of their orbits agree well, but once interior to the central few hundred kiloparsecs, the trajectories can diverge strongly. This divergence is quantified in Figure 9, where we plot the time evolution of the distance between a G-gal or its corresponding S-gal and the current position of the most massive G-gal. The latter marks the density center of the gas run. Galaxies follow similar trajectories in the two runs until

1996ApJ...472..460F

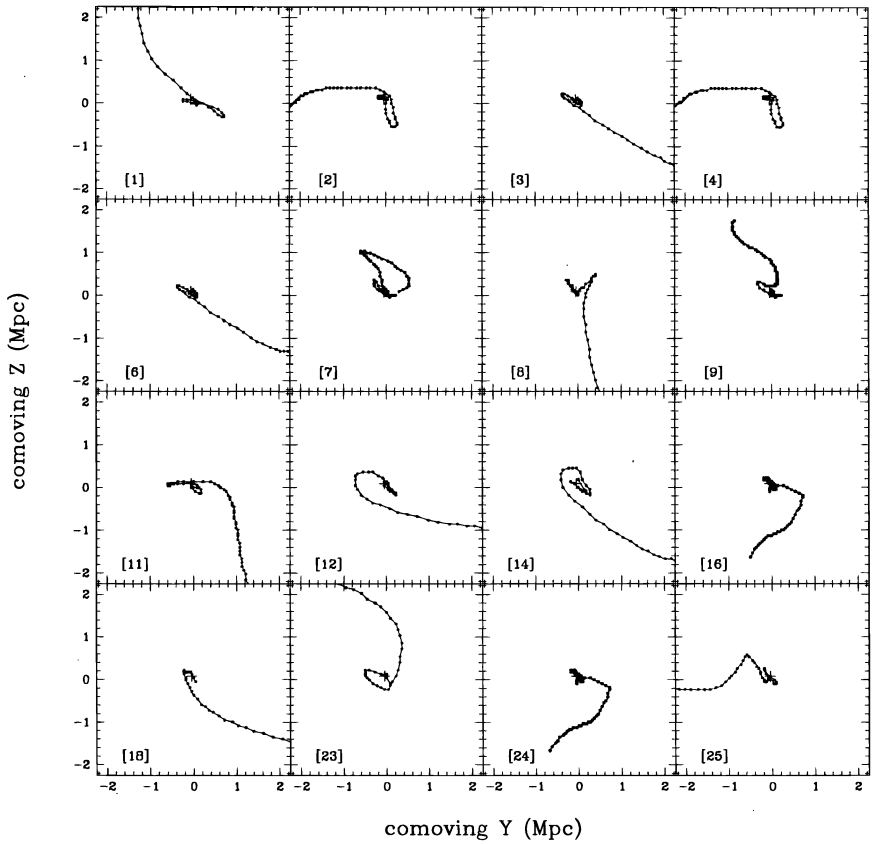

FIG. 8*a*

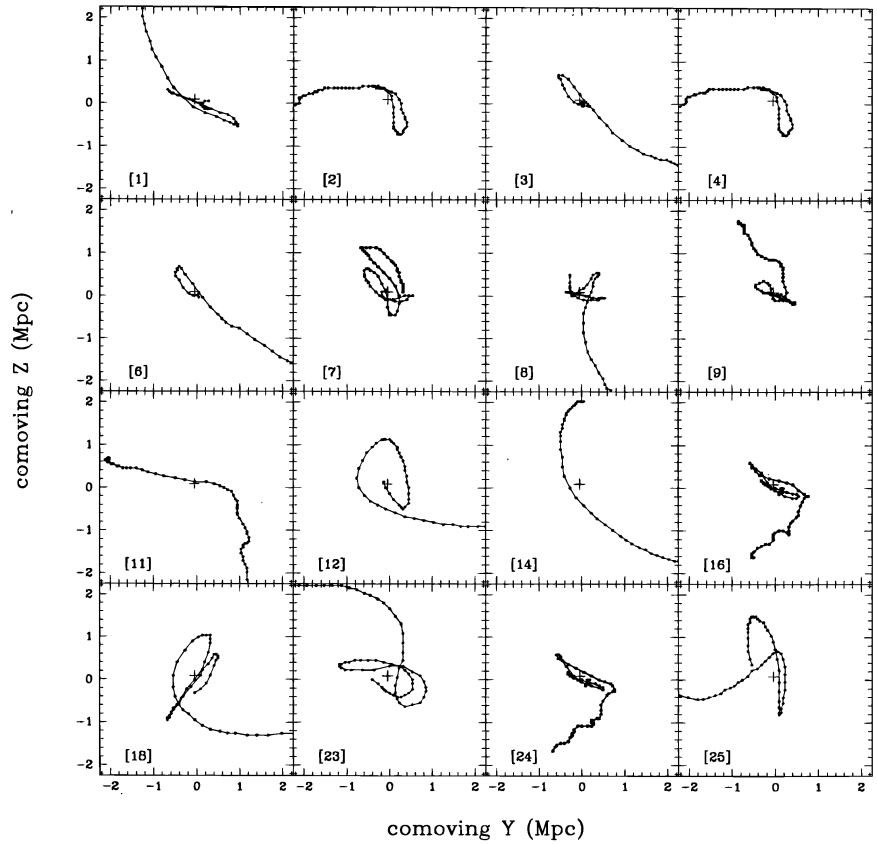

FIG. 8*b*

FIG. 8.—Orbits of (*a*) G-gals and (*b*) S-gals originally identified at $z = 0.7$ that end up in the cluster at the final epoch. The dots mark the positions, in comoving coordinates, of the center of mass of the particles belonging to a particular object at $z = 0.7$ at intervals of 10^8 yr. The cross marks the position of the center of the cluster at $z = 0$. The 16 most massive objects at $z = 0.7$ are shown, with the mass rank in brackets. Note the extreme differences in orbits for objects in the bottom two rows.

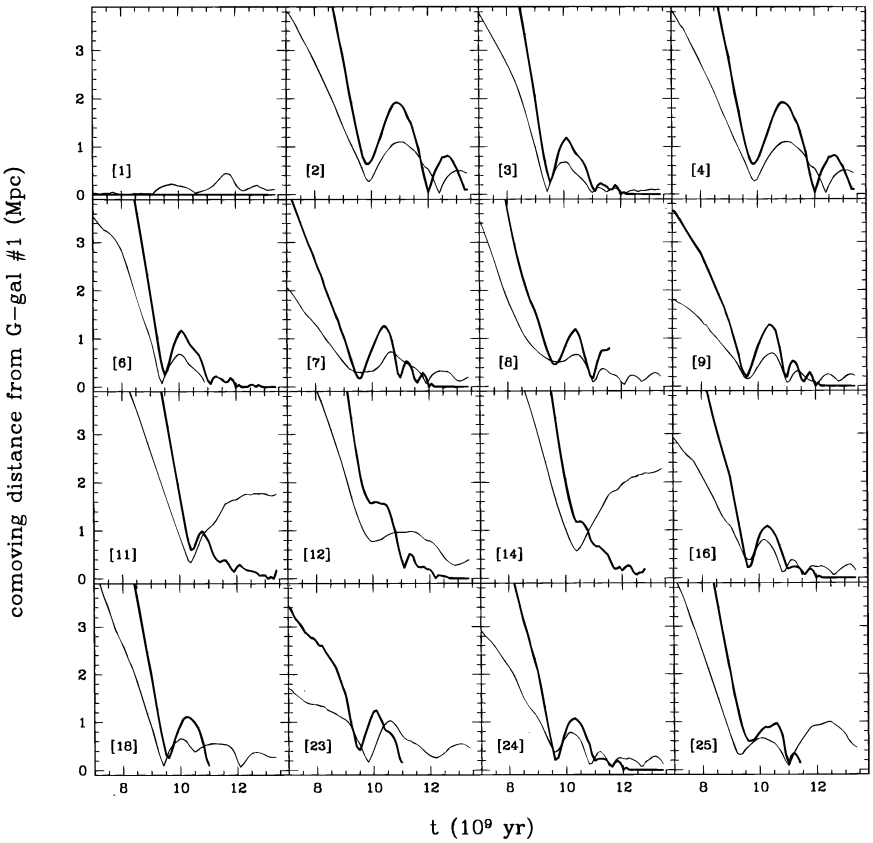

FIG. 9.—Comparison of the orbital properties of G- and S-gals shown in Fig. 8. The panels show the distance between the selected object and the position of the most massive G-gal (which tracks the position of maximum baryon density in the gas run), as a function of time. G-gals and S-gals track each other fairly well until their first periocentric passage.

they first pass near the cluster center. The most massive objects, shown in the top two rows of the figure, track fairly similar orbits confined to the inner few hundred kiloparsecs of the cluster. The lower mass sample in the bottom two rows show greater differences. In several instances (e.g., objects 11, 14, and 25), the G-gal is left behind near the center while the S-gal continues along an orbit that takes it back to radii $\gtrsim 2$ Mpc.

The braking of G-gals takes place largely in the inner few hundred kiloparsecs, where the gas density in the hot phase is high (~ 0.01 cm^{-3}) and where other G-gals occupy a substantial fraction of the volume. Direct G-gal collisions in the cluster core are responsible for some of this braking, along with an interaction with the hot, intracluster medium akin to ram pressure. This effect is also strongest in the dense core. A galaxy plowing into the hot phase density profile of Figure 6 would sweep up an amount of gas increasing as $r^{-1.2}$ at small radii. The induced drag on a galaxy will be important if the amount of mass swept up on its infall is comparable to its own mass. For a galaxy of radius r_g on an orbit with pericentric distance comparable to its radius, the swept mass on infall is $\sim 0.2\, M_{\rm ICM}(r_g/r_{\rm cl})^{0.8}$, where $M_{\rm ICM} = 1.2 \times 10^{14}\, M_\odot$ is the mass of hot gas within $r_{\rm cl}$. In the case of G-gals with radii $r_g \sim h_{\rm min} \sim 20$ kpc, this mass is $4 \times 10^{11}\, M_\odot$, equivalent to ~ 200 gas particles. Light G-gals on plunging orbits can therefore be trapped in the cluster core.

At larger radii, at which the hot phase density is low, ram pressure is dynamically unimportant. A legitimate concern is that numerical viscosity might enhance artificially the drag on G-gals. We have tested for this directly using simulations of a single small dense knot of cold gas in circular orbit within a polytrope. We chose the relative densities and temperatures of the two components to differ by about 3 orders of magnitude, as is the case for G-gals in our cluster. (These experiments were carried out using the tree-SPH code of Navarro & White [1994] with SPH parameters set to be similar to those of the code used here.) The effective drag (which comes entirely from the viscosity terms in the SPH scheme) is very small and is barely measurable over a few orbits.

Although most of the S-gals survive several pericentric passages, the number of such crossings is small. The crossing time of the present-day cluster at 4 Mpc, $t_c = \pi R^{3/2}(2GM)^{-1/2} \sim 6 \times 10^9$ yr, is comparable to the time elapsed since $z = 0.7$. The overall impression from this and previous plots is not one of an old, relaxed system of galaxies swarming around in a fixed cluster potential, but rather one of a young and dynamically evolving system.

As a result of their different merging histories, the final dominant objects in the centers of the two runs are very different. Figure 10 displays the merger histories of the most massive G-gal and S-gal, generated by linking groups from one time to the previous one, a time reversal of the procedure used to generate Figure 8. At $z = 0.7$, there are 24 objects which ultimately merge to form the dominant G-gal. In contrast, the largest S-gal forms from a single merger between two nearly equal mass objects whose relative orbit decays gradually over $\sim 2.5 \times 10^9$ yr.

To illustrate the dramatic consequences of these effects for the final appearance of the cluster, Figure 11 shows an image of the central 4.5 Mpc region for each representation

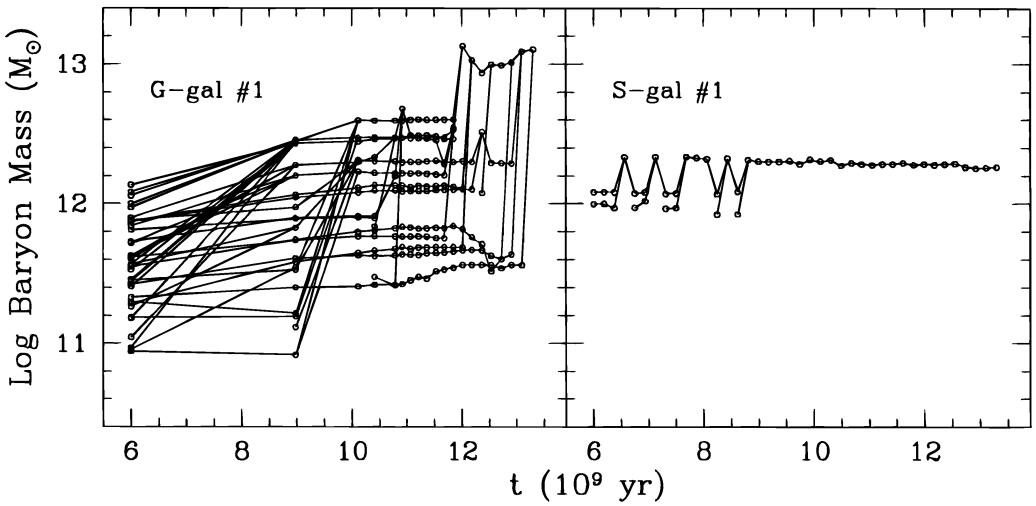

FIG. 10.—Merger histories of the most massive G-gal (*left*) and S-gal (*right*) identified at the final epoch. Merging is more extreme in the gasdynamic treatment.

of the galaxies. In these plots, the circle marking each galaxy has an area proportional to its mass. The largest G-gal dominates the "light" of the cluster and lies exactly on the cluster center. The largest S-gal is not nearly so dominant, and it lies about 400 kpc away from the projected cluster center. This figure shows clearly how the G-gals end up in a much more compact configuration than the S-gals.

To summarize, most G-gals that transverse the cluster core merge into the central object, whereas S-gals typically survive much longer and rarely merge. The apparent "overmerging" of the G-gals is consistent with the results of ESD, who found the G-gal number density to be antibiased in their cluster region. This and other previous SPH simulations that identified galaxies as cold, dense gas knots (e.g., Carlberg et al. 1990; Katz et al. 1992) thus provide a systematically biased description of the masses and clustering of galaxies. Our transformation of G-gals into S-gals is clearly too ad hoc to be considered a realistic model for galaxy formation; a reliable derivation of the masses and clustering of galaxies will require a much more careful treatment of galaxy formation than has been attempted by us (or by anyone else) so far.

4.3. *Hydrostatic Equilibrium*

The orbital properties illustrated in the preceding subsection determine the phase-space distribution of the various cluster populations and the extent to which they satisfy hydrostatic equilibrium. Figure 12 shows the radial and tangential velocities of the G-gals, the S-gals, the dark matter halos, and a subset of randomly chosen dark matter particles as a function of distance from the cluster center. The figure for the dark matter particles has the phase-wrapped appearance characteristic of systems formed via hierarchical clustering, with the (approximate) caustic surface of the most recently accreted mass separating the nonlinear portion of the cluster from the outer, quasi-linear infall regime at some radius r_{nl} (Rivolo & Yahil 1983; Bertschinger 1985). The phase-space diagram for the dark

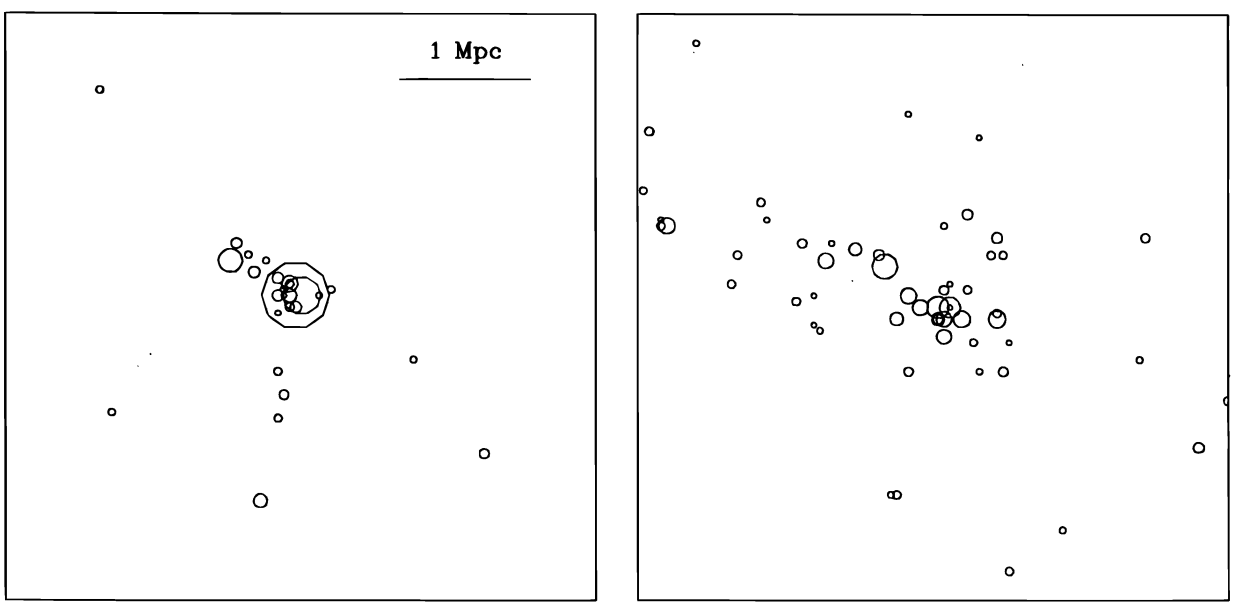

FIG. 11.—"Optical" appearance of the final cluster G-gals (*left*) and S-gals (*right*). A circle is plotted at the projected position of each galaxy, with radius proportional to the square root of its mass. The same scaling is used for both panels, with the smallest circles representing objects of 32 particles.

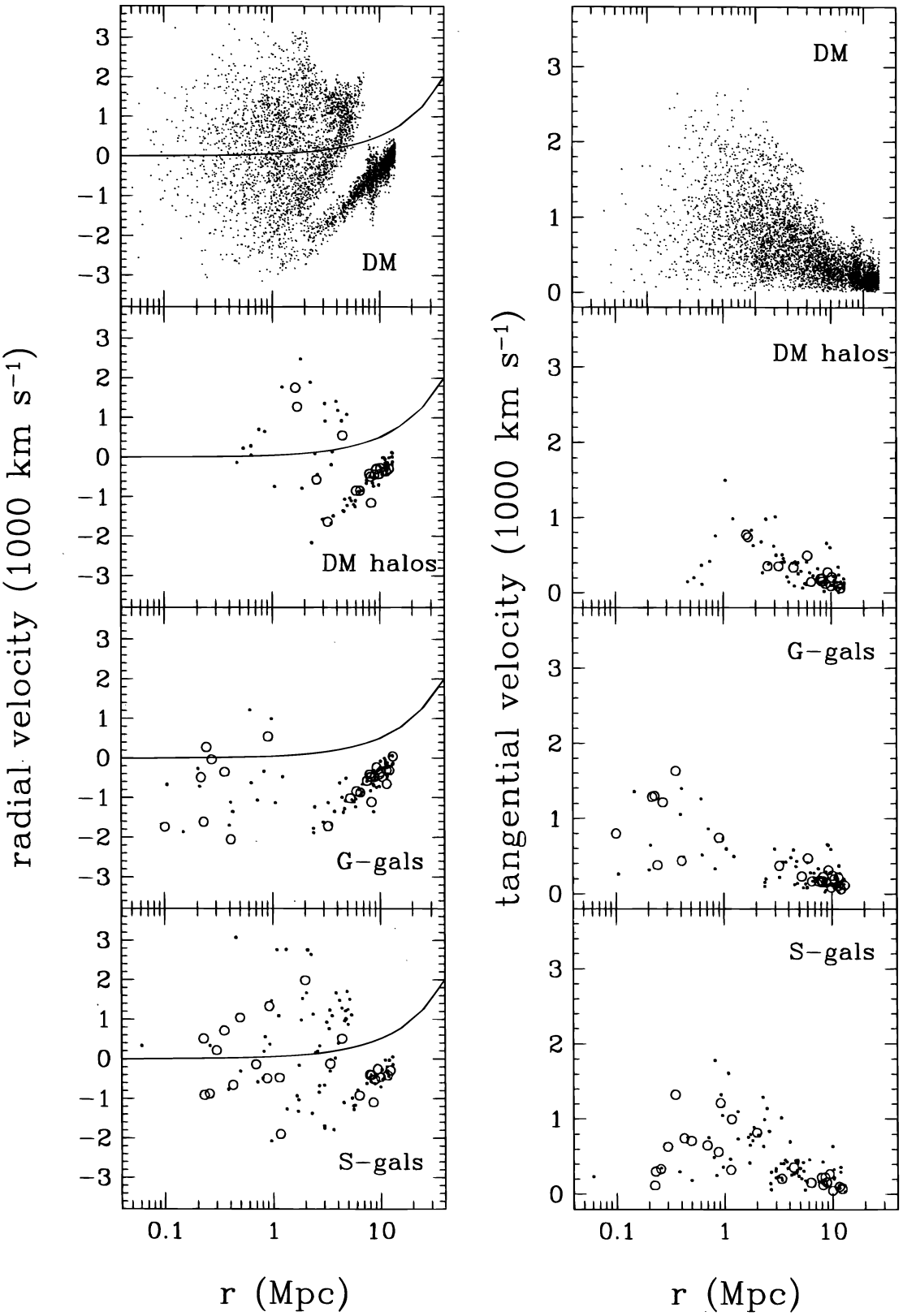

FIG. 12.—Phase-space diagrams for (a subset of) dark matter particles, dark matter halos, G-gals, and S-gals. The radial (*left*) and tangential (*right*) components of the velocity are plotted against radius from the cluster center at the final time. Circles represent massive objects with $N_p \geq 128$, while dots represent objects with $32 \leq N_p < 128$. Most dark matter halos in the nonlinear regime ($r \lesssim 6$ Mpc) are outflowing, while the G-gals in this regime are typically flowing inward. S-gals are the only population with an approximately hydrostatic signature.

matter indicates that the value of $r_{nl} \simeq 6$ Mpc is somewhat larger than our adopted cluster radius of 4 Mpc. The mean interior density contrast at r_{nl} is ~ 40.

The dark halos within r_{nl} are predominantly receding from the cluster center. The lack of halos falling in for the second time is due to tidal disruption during their first pericentric passage. In contrast, the G-gals within r_{nl} are nearly all moving radially inward. This is another manifestation of the viscous effects discussed earlier. Galaxies are effectively trapped as they fall through the cluster center, and they are prevented from moving back out to large radii. The S-gals are the only population that appears to have little or no net inflow or outflow within r_{nl}. Their distribution is similar to that of the dark matter, and they appear to be close to hydrostatic equilibrium.

4.4. *Binding Energy Analysis*

Further clarification of the physical processes that induce differences between the distributions of G-gals, S-gals, and dark matter halos can be obtained by tracking the evolution of their orbital binding energy. A variety of factors affect this energy. For example, in the "high peak model" galaxies are predicted to form more efficiently than average in protocluster regions and so may be born with systematically greater binding energy than random dark matter particles (Kaiser 1984; Davis et al. 1985; Bardeen et al. 1986). Subsequent dynamical processes can impose additional biases. Dynamical fiction causes massive galaxies to lose energy to the dark matter and to sink toward the cluster center, while galaxy merging can reduce the total number of galaxies and increase their luminosity. Differences present at early times may reasonably be ascribed to statistical "high peak" biases, whereas differences produced during and after cluster collapse must be of dynamical origin.

We calculate binding energies by convolving the mass distribution with a Plummer potential evaluated on a 128^3 mesh with a softening value of 0.45 Mpc. The potential at the position of each particle is then obtained by cloud-in-cell interpolation, and its binding energy is estimated by adding its specific kinetic energy. This procedure smooths over the contributions to the binding energy from very small-scale structures, allowing us to examine biases in the large-scale cluster potential.

Distributions of specific binding energy for "cluster particles" (i.e., particles that lie within 4 Mpc of the cluster center at $z = 0$) are plotted for several different epochs in Figure 13. (The binding energy is given in arbitrary units and is negative for bound particles.) The left panel compares the binding energy of the dark matter to that of the S-gals, while the right panel compares the binding energies of the G-gals and S-gals. (Only G- and S-gals with $N \geq 32$ were considered; note that the G-gal and S-gal histograms are mass weighted.) The collapse of the cluster is manifest in the dark matter plot as the rapid decrease in binding energy between $z = 0.7$ and $z = 0.3$. After this time, the potential well of the cluster continues to deepen, but a slower rate. The evolution of the binding energies of the S-gal and G-gal populations are qualitatively similar to this. However, already at $z = 0.7$, the binding energy distributions of these populations are biased toward more negative values than that of the dark matter. Since at this epoch the cluster has not yet collapsed, this bias may be interpreted as a property of the "initial conditions." Note that this is a significant effect. At the median of the distributions, the difference in binding energies between dark matter and S-gals at $z = 0.7$ is about 12%, compared to about 25% at $z = 0$.

By construction, the binding energy distributions of the G-gal and S-gal populations (right panel of Fig. 13) are almost identical at $z = 0.7$. (The small difference reflects the fact that there are a few S-gals that lie just outside 4 Mpc at $z = 0$, while their G-gal counterparts are just inside.) The collapse of the cluster at $z \simeq 0.3$ affects the two populations in a similar way, but by $z = 0$ the population of G-gals is considerably more tightly bound than the population of S-gals. This reflects the energy losses experienced by the G-gals through merging and viscous interactions and leads to their more centrally concentrated distribution relative to the S-gals, as discussed in § 4.2.

It is instructive to examine in some detail the origin of the differences between the binding energies of the dark matter

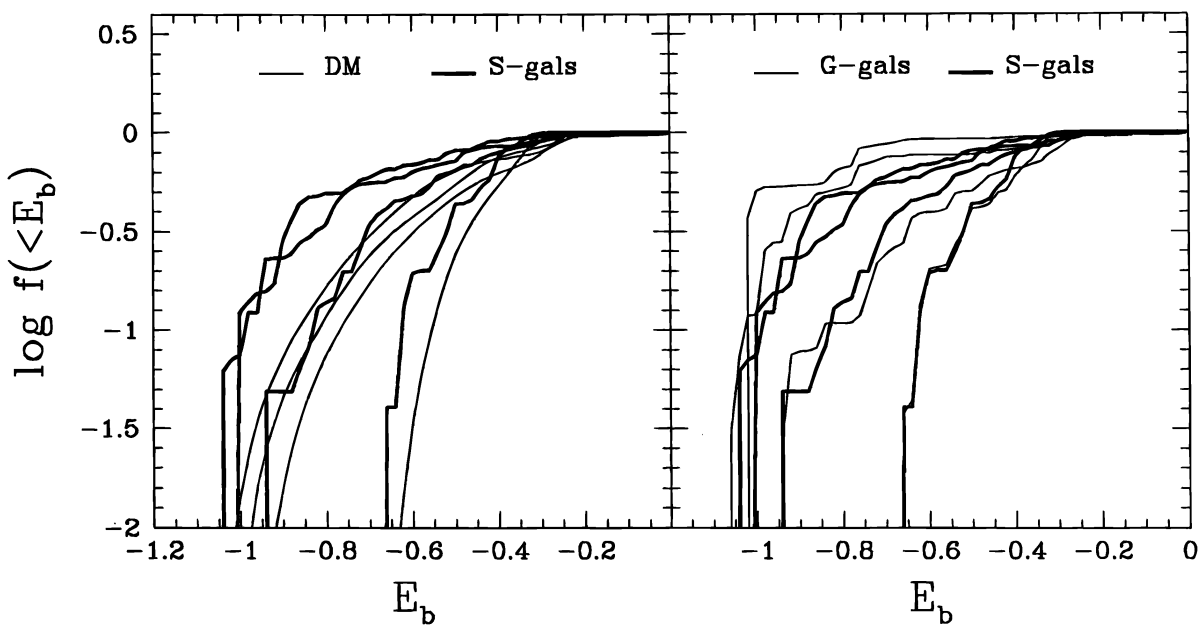

FIG. 13.—Cumulative binding energy distributions for dark matter particles, S-gals, and G-gals at redshifts (from right to left) $z = 0.7$, 0.3, 0.1, and 0. Only material found to be within 4 Mpc of the cluster center at the final time is considered.

and collapsed clumps. Particularly revealing are the trajectories, in binding energy space, of dark matter particles and individual clumps of similar initial binding energy. Figure 14 compares the binding energies at two different epochs of a randomly chosen subset of cluster dark matter particles. (The curves are logarithmically spaced isodensity contours and will be discussed below.) The top panel shows how the binding energies change between $z = 0.7$ and $z = 0.3$, the interval during which much of the cluster is assembled, but the evolution is relatively mild. The binding energies at these two epochs are well correlated, but with considerable scatter. Infalling material shows up as a cloud of points in the top right-hand corner of the diagram. The bottom panel of Figure 14 shows how the dark matter binding energy changes over the entire redshift range, $z = 0.7$ to $z = 0$. There are only minor differences between this and the top diagram, reflecting our earlier conclusion that the overall cluster potential evolves little between $z = 0.3$ and $z = 0$, even though major subcluster units are merging during this interval.

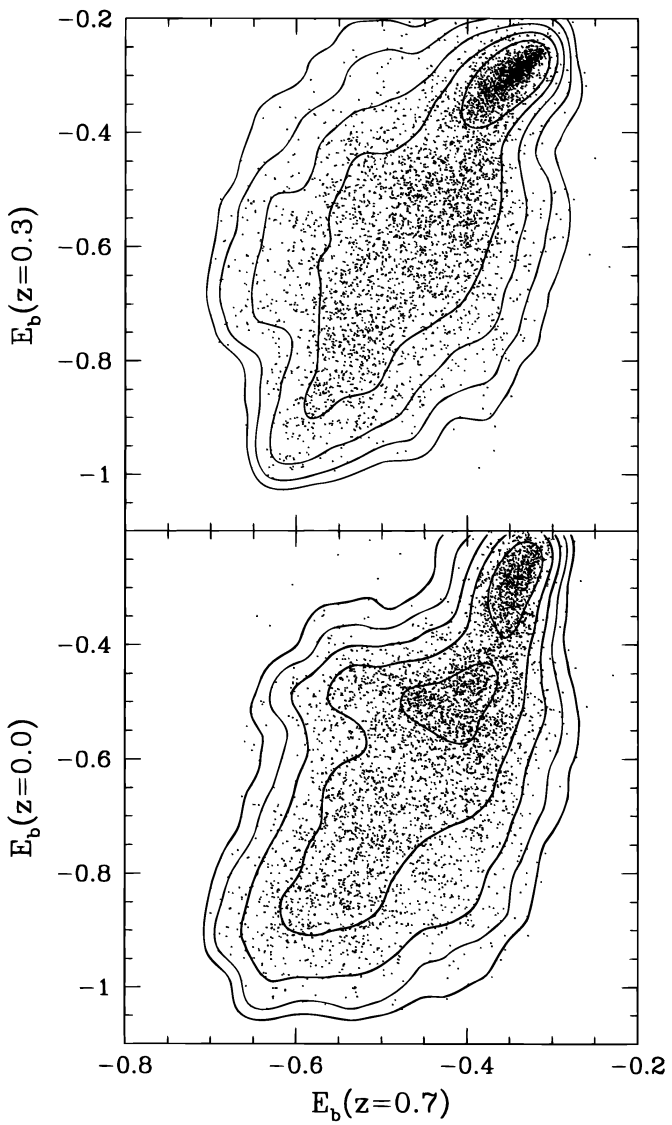

FIG. 14.—Binding energies of a randomly selected subset of cluster dark matter particles at $z = 0$ and 0.3 compared to $z = 0.7$. The isodensity contours tracing the distribution are used in Fig. 15.

Figure 15 contrasts the evolution of the dark matter with that of the G-gals and S-gals. All cluster particles that are members of a "galaxy" at both the plotted redshifts as well as at $z = 0$ are shown, while the dark matter is represented by the isodensity contours from Figure 14. The galaxies appear as distinct clumps. Clumps corresponding to galaxies that merge during the interval considered line up at a fixed binding energy at the later redshift. Many galaxy clumps are stretched in the vertical direction. In the case of the S-gals, this reflects heating by tidal and two-body effects between $z = 0.7$, when the cold gas was converted to stars, and the later epoch at which the clumps are examined again. In the case of the G-gals, vertical stretching reflects a recent merger that has temporarily led to a substantial increase in the random motions of gas particles within the merging clumps.

At $z = 0.7$, the distributions of S-gals and G-gals in Figure 15 are shifted slightly to the left relative to the dark matter distribution, reflecting the "initial" bias seen in Figure 13. Between $z = 0.7$ and $z = 0.3$, the G- and S-gals behave roughly like the dark matter, but there are some interesting differences of detail. For example, the G-gals become more distended than the S-gals, primarily because they undergo more mergers. (A notable exception is the most massive S-gal, which has a large velocity dispersion both at $z = 0.3$ and $z = 0$ and so a large vertical extent in the plots.) In addition, by $z = 0.3$, a number of mergers of G-gals are apparent that have so S-gal counterparts.

The lower panels of Figure 15, which compare binding energies at $z = 0.7$ and at $z = 0$, reveal quite dramatic differences among the three components. Material that had the same binding energy at $z = 0.7$ can end up with an entirely different binding energy at $z = 0$, depending on whether it is dark matter, an S-gal, or a G-gal. The segregation relative to the dark matter is much greater for the G-gals than for the S-gals, but even the S-gals show a marked tendency for the largest clumps to end up near the center of the potential well. Virtually all the G-gals that survive until $z = 0$ have merged into two dominant objects; the only other surviving objects were loosely bound initially and are currently falling in for the first time (see Fig. 12 above). The S-gals are spread over a larger range of binding energy at $z = 0$ than the G-gals, but they also show a marked deficit of moderately bound members compared to the dark matter. The distributions of G-gals, S-gals, and dark matter are similar in the outer parts of the cluster, where the ridge line of accreting objects is visible in all three components. These plots suggest that most of the segregation between massive clumps and dark matter occurs after $z = 0.3$, when much of the cluster material is already in place.

These diverging evolutionary trajectories presumably reflect the different interactions to which the three components are subject. S-gals experience only gravity, but their relatively high mass causes them to lose energy to the diffuse dark matter background. It seems appropriate to refer to this mechanism as dynamical friction even though the transfer of energy between the populations in a lumpy and rapidly changing environment does not conform to the standard picture in which a massive object spirals gradually to the center of a quasi-static potential well. The stronger biases apparent for the more massive S-gals (see Table 3) favor this interpretation, since dynamical friction should increase linearly with galaxy mass. The G-gals also experience dynamical friction, but their evolution is influenced

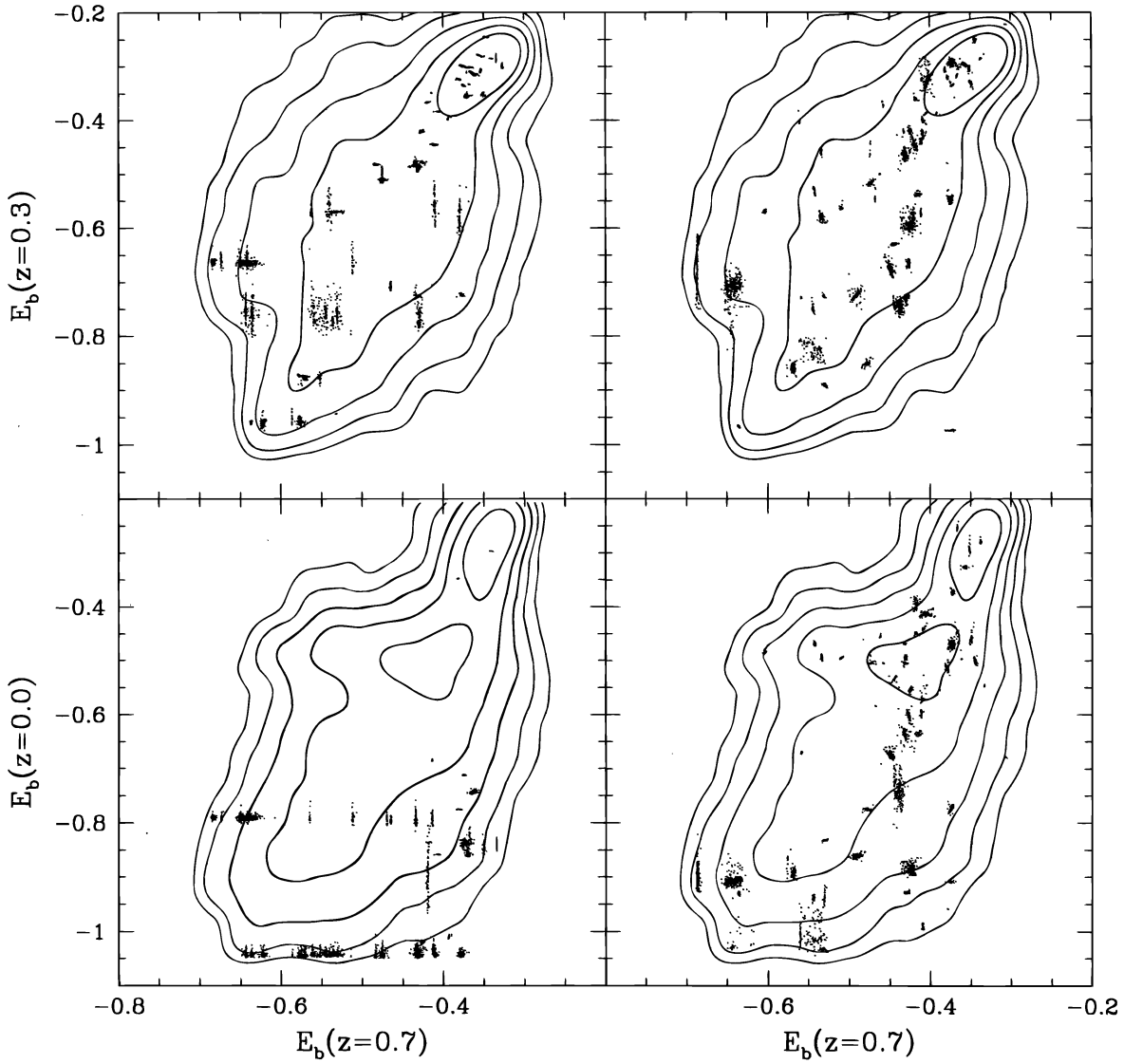

FIG. 15.—Binding energies of the particles in the cluster G-gals (*left*) and S-gals (*right*) at $z = 0$ and $z = 0.3$ compared to $z = 0.7$. All the particles plotted belonged to a "galaxy" at $z = 0$ and at the two redshifts shown. The contours represent the dark matter distribution from Fig. 14.

further by the viscous effects that enhance the tendencies toward merging and gravitational settling. These processes combine with the bias present before collapse to produce the strong mass segregation seen in Figure 11 and an associated velocity bias, which we discuss in § 4.5 below. As we shall see, these biases cause a standard virial analysis to underestimate substantially the mass of the cluster.

4.5. *Virial Mass Estimates*

Dynamical estimates of the masses of rich galaxy clusters, based on the application of the virial theorem or of the equations of stellar hydrodynamics, yield mass-to-light ratios which are typically a factor of 3–5 smaller than the ratio of the closure density to the (appropriately weighted) observed mean luminosity density in galaxies (Geller 1984; The & White 1986; Merritt 1987). Proponents of a universe with closure density have long argued that this discrepancy may reflect a bias in the distribution of galaxies toward rich clusters, an idea that was developed formally in the "high peak" model for biased galaxy formation (Davis et al. 1985; Bardeen et al. 1986). Partial support for this view was provided by the collisionless simulations of White et al. (1987a) and Frenk et al. (1988), which showed explicitly how massive galactic halos in the standard CDM model form preferentially in protocluster regions. Other workers (Barnes 1985; Evrard 1987; West & Richstone 1988) pointed out that a further bias could result if dynamical friction segregated galaxies from mass within a cluster. In § 4.4, we showed that all these biases are indeed present in our simulated cluster.

For real clusters, masses are commonly estimated using the virial theorem, which may be written in the form (Heisler, Bahcall & Tremaine 1985)

$$M_{\rm VT} = \frac{3\pi N}{2G} \frac{\sum_i v_{p,i}^2}{\sum_{i<j} R_{ij}^{-1}}, \tag{3}$$

where $v_{p,i}$ is the line-of-sight velocity and R_{ij} is the projected separation of a pair of galaxies. Tables 2 and 3 give the mass estimates obtained from this formula using the kinematic data for G- and S-gals within projected radii of 2, 4, and 6 Mpc. Results are given for objects in two separate mass ranges. The quantities $\sigma_{\rm gal}$ and $\sigma_{\rm DM}$ are one-dimensional velocity dispersions, obtained by averaging over three orthogonal projections. The masses quoted are also the

TABLE 2

CLUSTER MASS ESTIMATES USING G-GALS

N_p	r_{cut} (Mpc)	N_{gal}	σ_{gal} (km s^{-1})	r_h (kpc)	$\sigma_{gal}/\sigma\rho_{DM}$	$M_{VT}/M_{true}(<r_{cut})$
32.....	2.0	23	447	304	0.82	0.41
	4.0	31	457	480	0.84	0.44
	6.0	42	451	784	0.83	0.56
128.....	2.0	9	451	190	0.83	0.27
	4.0	10	469	234	0.86	0.23
	6.0	11	465	282	0.86	0.22

mean of three projections and are given in terms of the true total cluster mass within a sphere of the given radius.

All the virial mass estimates in Tables 2 and 3 underestimate the true mass by an amount that depends on the type of object considered. The heavy G-gals give the smallest virial mass ($\sim$25% of the true value), and the lighter S-gals give the largest ($\sim$75% of the true value). These underestimates result from a combination of two effects. First, all populations of galaxies are "cooler" than the dark matter. As shown in the sixth column of the tables, the magnitude of this "velocity bias" is similar for all populations, ranging from $\sim$30% for the heavier S-gals to $\sim$20% for the lighter S-gals. The second contribution comes from the spatial distributions of the tracer populations that differ markedly among the different types of object. As discussed in § 4.1, all populations, except the lighter S-gals, are more centrally concentrated than the mass. The ratio of their median radius to the half-mass radius of the dark matter ranges from 0.25 for the heavier G-gals to $\sim$1 for the lighter S-gals. Since the virial mass estimate is proportional to $R\sigma_{gal}^2$, the velocity bias contributes 20%–60% of the factor by which the true mass is underestimated, and the spatial bias contributes the rest.

When applied to the galaxies in our simulation, the standard "cluster M/L" argument underestimates the mean cosmological density, Ω, by a factor that is at least as large as the factor by which the true cluster mass is underestimated. This is because the mass fraction in galaxies is also biased high relative to the dark matter in the cluster (see § 3.2). For example, the mass fractions in lighter and heavier S-gals are biased by factors of 1.5 and 2, respectively, and if these are assumed representative of the global values, these populations yield Ω estimates of 0.5 and 0.12, respectively. Unfortunately, we cannot determine reliably the global bias in the cluster "light" from our simulation. The region we have modeled is dominated by the cluster, and so radial gradients extend outward from the cluster center all the way to the simulation boundary. In addition, the apodization required at the boundary affects fluctuations in roughly 20% of the volume but, since only wavelengths much larger than galaxy scales are affected, this is unlikely to reduce significantly the number of galaxies in the outer parts of the simulation volume. Our estimates of Ω strongly suggest that the "M/L argument" applied to clusters in an $\Omega = 1$ universe may yield misleadingly low estimates of Ω. For the G-gal population and for the galaxy tracers used in earlier work (Carlberg & Couchman 1989; Katz et al. 1992; ESD), a similar bias could be blamed on unrealistically strong viscous interactions, but these have no effect on the distribution of our S-gals.

TABLE 3

CLUSTER MASS ESTIMATES USING S-GALS

N_p	r_{cut} (Mpc)	N_{gal}	σ_{gal} (km s^{-1})	r_h (kpc)	σ_{gal}/σ_{DM}	$M_{VT}/M_{true}(<r_{cut})$
32.....	2.0	35	467	550	0.86	0.72
	4.0	59	450	948	0.83	0.76
	6.0	77	431	1322	0.79	0.79
128.....	2.0	13	371	322	0.68	0.28
	4.0	15	374	406	0.69	0.24
	6.0	16	368	456	0.68	0.20

5. DISCUSSION

The differences of behavior that we find among our three simulations are a graphic illustration of how relatively small changes in the numerical approach adopted to study galaxy and cluster formation can lead to large quantitative and qualitative changes in the results. The failure of our original experiment to produce a significant number of galaxies demonstrates that, near the dynamic range limit of a gas-dynamics code, lack of resolution can reduce significantly the ability of gas clumps to cool and so to make "galaxies"; a relatively modest enhancement of the cooling rate increased the number of dense clumps at the final time by 2 orders of magnitude. While the amount of cold dense material in "galaxies" appears much more plausible in this second gas simulation, it is possible that resolution effects are still causing a major underestimate of the amount of cold dense gas. ESD came to a similar conclusion when comparing the cold gas fraction in their own experiment with the much smaller values found in simulations carried out with grid-based hydrodynamics techniques and lower resolution SPH models. Analytic models for galaxy and cluster formation are not, of course, subject to such resolution limitations, and it has long seemed clear that radiative or hydrodynamical heating of pregalactic gas is required to prevent almost all of it from cooling, and so to explain the large amount of diffuse gas observed in galaxy clusters (White & Rees 1978; Cole 1991; White & Frenk 1991; Blanchard, Valls-Gabaud, & Mamon 1992; Kauffmann et al. 1993; Cole et al. 1994).

Once gas is able to cool and settle into dense clumps, then all experiments agree that only a small fraction of it is ever reheated or dispersed into the dilute phase by the disruptive effects of later gravitational and hydrodynamical evolution. The high densities attained (which are similar to the observed densities of real galaxies) are sufficient to protect the clumps against tidal or ram pressure stripping. This confirms both the original conjecture of White & Rees (1978) and the earlier numerical results of Carlberg (1988), Katz et al. (1992), and ESD. Dissipative effects allow galaxies to survive individually beyond the consolidation of their dark halos into a single monolithic cluster halo.

Unfortunately, while both our simulations agree that galaxy disruption is relatively unimportant, they give very different predictions for the strength of frictional drag on galaxy orbits and for the amount of galaxy merging. The latter processes are both much stronger in a simulation in which galaxies remain gaseous than in one in which they are turned into stars. Viscous drag affects gaseous "galaxies" only in the central regions of the cluster, and their tendency to merge after a close encounter or collision is much greater than that for stellar galaxies of the same size and mass. These effects cause the galaxies in our "gas" simulation to merge rapidly into the central dominant object, and they

lead to a final galaxy population that has little resemblance to that seen in most real clusters. It remains possible that, for the minority of clusters that do harbor dominant galaxies containing a large fraction of the total cluster light, mergers of gas-rich progenitors may have played an important role.

By comparison, the evolution of the galaxy population after $z = 0.7$ in our "star" simulation is much milder, and the final system appears a much better model for real systems. It is nevertheless important to remember that at $z > 0.7$ the galaxies are 100% gaseous in this simulation also; their mass function and their spatial distribution may therefore already have been affected significantly by the artificial effects we have just discussed.

However, it is also possible that the final state of the "star" simulation is determined primarily by dynamical effects occurring after $z = 0.7$ (since this period encompasses the main collapse of the cluster) and that these effects are treated relatively accurately in the model. The galaxies in this model appear to be approximately in equilibrium in the central regions by $z = 0$, even though the crossing time in the cluster is comparable to its dynamical age. Their density distribution is more centrally concentrated than that of the dark matter and, beyond the inner 150 kpc, the profile of the lighter galaxies is quite similar to the profiles observed in real clusters. The stellar "galaxies" exhibit a mild velocity bias and a moderate segregation by mass. Both these properties are primarily the outcome of dynamical friction. Thus, our simulations lead us to expect some degree of luminosity segregation in real clusters. This is a difficult to measure beyond the central regions of real clusters (Capelato et al. 1980; Kent & Gunn 1982; Sodre et al. 1992; Biviano et al. 1992), but large spectrophotometric surveys are beginning to show convincing evidence for it (den Hartog & Katgert 1996). In our simulated cluster, mass segregation among the S-gals is confined mostly to the central regions; beyond a few hundred kiloparsecs their distribution is only weakly dependent on mass.

Applying the virial theorem to the "stellar galaxies" in our simulation leads to an underestimate of the cluster mass that can be quite significant if only the most massive galaxies are used. A further bias is present because more galaxies form per unit mass in the cluster than outside it. Although the strength of this effect cannot be measured accurately in our simulations, it contradicts the common assumption that the mass-to-light ratio of clusters can be identified with the universal value. Thus, a standard M/L analysis of our simulation returns an estimate of Ω in the range 0.1–0.5, even though the true value is unity.

In many respects our simulated cluster appears a plausible match to real clusters. Its bulk X-ray properties are quite similar to those observed, confirming and extending previous results from models in which the intergalactic medium was treated as a nonradiative gas. The inclusion of cooling and an admittedly oversimplified prescription for turning cold gas into stars produces a population of galaxies that has many similarities to observed populations. Although the treatment of galaxy formation still needs much improvement, these successes are encouraging and suggest that a viable model for the formation of galaxy clusters is indeed attainable within hierarchical clustering theories such as the one explored in this paper.

We would like to thank Julio Navarro for useful discussion and for carrying out some of the tests discussed in § 4.2. This work was supported by a NATO Collaborative Research Grant and by PPARC (C. S. F. and S. D. M. W.), NASA grant NAGW-2367 (A. E. E.) and a grant of supercomputer time at the San Diego Supercomputer Center sponsored by NSF. The hospitality of the Aspen Center for Physics, where this paper was begun, and the Institute for Theoretical Physics at UC, Santa Barbara, where this paper was finished, is gratefully acknowledged. This research was supported in part by the National Science Foundation under grant no. PHY89-04035.

REFERENCES

Bardeen, J. M., Bond, J. R., Kaiser, N., & Szalay, A. S. 1986, ApJ, 304, 15
Barnes, J. 1985, MNRAS, 215, 517
Bertschinger, E. 1985, ApJS, 58, 39
Biviano, A., Girardi, M., Giuricin, G., Mardirossian, F., & Mezzetti, M. 1992, ApJ, 396, 35
Blanchard, A., Valls-Gabaud, D., & Mamon, G. A. 1992, A&A, 264, 365
Bryan, G. L., Cen, R., Norman, M. L., Ostriker, J. P., & Stone, J. M. 1994, ApJ, 428, 405
Capelato, H. V., Gerbal, D., Mathez, G., Mazure, A., Salvador-Solé, E., & Sol, H. 1980, ApJ, 241, 521
Carlberg, R. G. 1988, ApJ, 332, 26
Carlberg, R. G., & Couchman, H. M. P. 1989, ApJ, 340, 47
Carlberg, R. G., Couchman, H. M. P., & Thomas, P. A. 1990, ApJ, 352, L29
Cen, R., & Ostriker, J. P. 1992a, ApJ, 393, 22
———.1992b, ApJ, 399, L113
Cole, S. 1991, ApJ, 367, 45
Cole, S., Argón-Salamanca, A., Frenk, C. S., Navarro, J. F., & Zepf, S. 1994, MNRAS, 271, 781
Crone, M. M., Evrard, A. E., & Richstone D. 1994, ApJ, 434, 402
Davis, M., Efstathiou, G. P., Frenk, C. S., & White, S. D. M. 1985, ApJ, 292, 371
den Hartog, R., & Katgert, P. 1996, MNRAS, 279, 349
Dubinski, J., & Carlberg, R. G. 1991, ApJ, 378, 496
Efstathiou, G. 1992, MNRAS, 256, 43p
Efstathiou, G., Davis, M., Frenk, C. S., & White, S. D. M. 1985, ApJS, 57, 241
Efstathiou, G., Frenk, C. S., White, S. D. M., & Davis, M. 1988, MNRAS, 235, 715
Evrard, A. E. 1987, ApJ, 316, 36
———.1988, MNRAS, 235, 911
———.1990, ApJ, 363, 349
Evrard, A. E., Mohr, J. J., Fabricant, D. G., & Geller, M. J. 1993, ApJ, 419, L12
Evrard, A. E., Summers, F., & Davis, M. 1994, ApJ, 422, 11 (ESD)
Frenk, C. S., White, S. D. M., Efstathiou, G., & Davis, M. 1988, ApJ, 327, 507
———.1990, ApJ, 351, 10
Geller, M. J. 1984, Comments Astrophys. Space Sci., 2, 47
Heisler, J., Bahcall, J., & Tremaine, S. 1985, ApJ, 298, 8
Kaiser, N. 1984, ApJ, 284, L9
Kang, H., et al. 1994, ApJ, 430, 83
Katz, N., Hernquist, L., & Weinberg, D. H. 1992, ApJ, 399, 109
———.1995, preprint
Katz, N., & White, S. D. M. 1993, ApJ, 412, 455
Kauffmann, G., & White, S. D. M. 1993, MNRAS, 261, 921
Kauffmann, G., White, S. D. M., & Guiderdoni, B. 1993, MNRAS, 264, 201
Kent, S., & Gunn, J. 1982, AJ, 87, 945
Lacey, C. G., & Cole, S. 1993, MNRAS, 262, 627
Loveday, J., Peterson, B. A., Efstathiou, G., & Maddox, S. J. 1992, ApJ, 390, 338
Marzke, R. O., Huchra, J. P., & Geller, M. J. 1994, ApJ, 428, 43
Merritt, D. 1987, ApJ, 313, 121
Metzler, C. A., & Evrard, A. E. 1994, ApJ, 437, 564
Navarro, J. F., Frenk, C. S., & White, S. D. M. 1995, MNRAS, 275, 720
Navarro, J. F., & White, S. D. M. 1994, MNRAS, 267, 401
Pearce, F., Thomas, P. A., & Couchman, H. M. P. 1994, MNRAS, 268, 953
Peebles, P. J. E. 1970, AJ, 75, 15
Quinn, P. J., Salmon, J. K., & Zurek, W. 1986, Nature, 322, 329
Richstone, D. O., Loeb, A., & Turner, E. L. 1992, ApJ, 393, 477
Rivolo, A. R., & Yahil, A. 1983, ApJ, 274, 474
Roettiger, K., Burns, J., & Loken, C. 1993, ApJ, 407, L53
Schombert, J. M. 1988, ApJ, 328, 475
Sodre, L., Mazure, A., Capelato, H., & Proust, D. 1992, MNRAS, 259, 233
Summers, F. J. 1993, Ph.D. thesis, Univ. California, Berkeley
The, L., & White, S. D. M. 1986, AJ, 92, 1248
Thomas, P., & Couchman, H. M. P. 1992, MNRAS, 257, 11

Tsai, J. C., Katz, N., & Bertschinger, E. 1994, ApJ, 423, 553
West, M. J., Dekel, A., & Oemler, A. J. 1987, ApJ, 316, 1
West, M. J., & Richstone, D. O. 1988, ApJ, 335, 532
White, S. D. M. 1976, MNRAS, 177, 717
White, S. D. M., Davis, M., Frenk, C. S., & Efstathiou, G. 1987a, Nature, 330, 451
White, S. D. M., & Frenk, C. S. 1991, ApJ, 379, 25
White, S. D. M., Frenk, C. S., Davis, M., & Efstathiou, G. 1987b, ApJ, 313, 505
White, S. D. M., Navarro, J. F., Evrard, A. E., & Frenk, C. S. 1993, Nature, 336, 429
White, S. D. M., & Rees, J. J. 1978, MNRAS, 183, 341
Wilson, G., Cole, S., & Frenk, C. S. 1996, MNRAS, 280, 199